

# Rheology of a coaxial shear zone in the Virginia Blue Ridge: Wet quartzite dislocation creep at $\sim 250\text{--}280\text{ }^{\circ}\text{C}$

John S. Singleton<sup>a,\*</sup>, Jeffrey M. Rahl<sup>b</sup>, Kenneth S. Befus<sup>c</sup>

<sup>a</sup> Department of Geosciences, Colorado State University, Fort Collins, CO, 80523, USA

<sup>b</sup> Department of Geology, Washington and Lee University, Lexington, VA, 24450, USA

<sup>c</sup> Department of Geosciences, Baylor University, Waco, TX, 76798, USA

## ARTICLE INFO

### Keywords:

Rheology  
Hydrolytic weakening  
Brittle-plastic transition  
Coaxial flattening  
Antietam Formation  
Blue Ridge

## ABSTRACT

Cambrian quartzite along the western margin of the Blue Ridge near Front Royal, Virginia records significant penetrative strain under subgreenschist-facies conditions. Strain analyses of the quartzite indicate general flattening and octahedral shear strain values up to 1.25 (X:Z up to 5.7:1). Samples with X:Z as low as 1.5:1 have crystallographic preferred orientations that record a dominance of basal  $\langle a \rangle$  slip and patterns consistent with coaxial flattening. In most samples quartz has undergone minor amounts of dynamic recrystallization with mean grain sizes  $\sim 4\text{--}5\text{ }\mu\text{m}$ . Locally, the quartzite is brittily deformed, and subgrains and recrystallized bulges are present along fractures and extinction bands. Fluid-inclusion planes and fluid inclusions along deformation lamellae are abundant, and quartz FTIR analyses yield average H:10<sup>6</sup>Si values of 1100–3300, indicating fluid flow and high intragranular water content during deformation. Higher strain samples generally record lower water contents, which may indicate that fluids migrated to grain boundaries during deformation. Dissolution microstructures are rare in high strain samples, and we interpret most strain to have been accommodated by dislocation creep. Thermal modeling of zircon low-temperature thermochronology data coupled with quartz *c*-axis opening angle thermometry suggest deformation temperatures were likely  $\sim 250\text{--}280\text{ }^{\circ}\text{C}$ . These deformation temperatures are lower than what is typically considered the brittle-plastic transition in quartz. We attribute localization of this high strain zone and dislocation creep at these temperatures to hydrolytic weakening and a relatively low strain rate estimated to be  $\sim 10^{-15}\text{ s}^{-1}$ .

## 1. Introduction

The rheology of quartz is fundamental to understanding deformation of continental crust. Given that quartz commonly forms an interconnected weak phase in mid-crustal shear zones, quartz rheology may govern crustal strength, and strength profiles commonly rely on quartzite flow laws. Quartz deformation conditions near the brittle-plastic transition (BPT) are particularly important. Peak strength of the crust resides at the BPT (e.g., Sibson, 1983; Kohlstedt et al., 1995; Behr and Platt, 2014), which may act as the primary load-bearing region, controlling the state of stress throughout the crust and affecting the distribution, rate, and style of deformation.

Several factors influence quartz deformation near the BPT, including strain rate, temperature, differential stress, and water content. Unfortunately, accurately quantifying these parameters in naturally deformed rocks is difficult, and deformation experiments must be carried out at

strain rates  $>4$  orders of magnitude faster and temperatures significantly higher than those recorded by natural shear zones. The transition from dominantly brittle fracturing to intracrystalline plastic flow in naturally deformed quartz is commonly presented as temperature-dependent, with  $\sim 300\text{ }^{\circ}\text{C}$  widely referenced as the transition temperature (e.g., Sibson, 1977; Passchier and Trouw, 2005; Fossen, 2016). In crustal-scale fault zones the BPT temperature should increase with increasing strain rate, increasing pore fluid pressure, and decreasing intragranular water content. In addition, the BPT is predicted to occur at higher stresses and lower temperatures in a thrust fault regime compared to strike-slip and normal fault regimes, although constraints from ductile shear zones do not always support this prediction (e.g., Behr and Platt, 2014). Dislocation creep conditions just below the BPT in normal-sense shear zones deformed at strain rates of  $10^{-11}\text{ s}^{-1}$  to  $10^{-14}\text{ s}^{-1}$  range from  $\sim 300\text{ }^{\circ}\text{C}$  to  $350\text{ }^{\circ}\text{C}$  with peak stresses recorded by mean dynamically recrystallized grain sizes of  $\sim 4\text{--}20\text{ }\mu\text{m}$  (Gueydan et al., 2005; Behr and Platt, 2011,

\* Corresponding author.

E-mail address: [john.singleton@colostate.edu](mailto:john.singleton@colostate.edu) (J.S. Singleton).

<https://doi.org/10.1016/j.jsg.2020.104109>

Received 27 February 2020; Received in revised form 31 May 2020; Accepted 1 June 2020

Available online 23 June 2020

0191-8141/© 2020 Elsevier Ltd. All rights reserved.

2013; Gottardi and Teyssier, 2013; Singleton et al., 2018). Estimates of the BPT temperature in quartz mylonites from strike-slip shear zones deformed at strain rates of  $10^{-12}$  s $^{-1}$  to  $10^{-14}$  s $^{-1}$  range from  $\sim 280$  °C to 310 °C, with peak stresses recorded by a mean dynamically recrystallized grain size of  $\sim 5$ – $7$   $\mu\text{m}$  (Stöckhert et al., 1999; Stipp et al., 2002, Stipp and Kunze, 2008; Faleiros et al., 2010). Several studies of quartz deformation in thrust regimes deformed at strain rates of  $10^{-12}$  s $^{-1}$  to  $10^{-16}$  s $^{-1}$  document crystal plastic strain near the BPT at temperatures  $\leq 300$  °C and mean recrystallized grain sizes  $\sim 5$ – $15$   $\mu\text{m}$  (Voll, 1976; Koch and Masch, 1992; Dunlap et al., 1997; Küster and Stöckhert, 1999; van Daalen et al., 1999; Hirth et al., 2001; Trepmann and Stöckhert, 2009; Kidder et al., 2012; Kjöll et al., 2015). The quartz BPT temperature in Alpine thrust nappes has been estimated to be  $\sim 270$ – $275$  °C (Voll, 1976; van Daalen et al., 1999), and several studies of thrust zones suggest that quartz crystal-plastic strain may have occurred at temperatures as low as  $\sim 250$  °C (Dunlap et al., 1997; Trepmann and Stöckhert, 2009; Kidder et al., 2012). Given that significant crystal-plastic strain in quartz is typically thought to require temperatures  $\geq \sim 300$  °C, understanding the conditions that facilitate lower-temperature strain commonly inferred in thrust systems is important. Fluids may play an important role in accommodating this low-temperature strain, as hydrolytic weakening of quartz promotes dislocation glide at lower temperatures (e.g., Griggs, 1967; Blacic, 1975). However, few studies of natural shear zones have quantified both deformation conditions and quartz intragranular water content near the BPT. The ability of quartz to undergo dislocation creep at such low temperatures has important implications for the strength and behavior of crustal-scale fault zones. In thrust regimes décollements commonly record deformation in the  $\sim 250$ – $300$  °C range, so the rheology of quartz under these conditions may exert a significant influence on critical taper and the architecture of orogenic wedges.

In this study we investigate the strain and rheological behavior of quartzite deformed near the BPT in subgreenschist-facies conditions. We evaluate strain geometry and magnitude, deformation mechanisms, quartz crystallographic preferred orientations, water content, and the thermal history of this quartzite with the goal of constraining deformation conditions and understanding how significant penetrative strain may be accommodated below typical quartz BPT temperatures.

## 2. Geologic setting

The Blue Ridge Mountains in the eastern United States comprise a major basement massif in the Appalachian orogen. Blue Ridge basement rocks record a complex tectonic history that includes high-grade regional metamorphism and plutonism during the Mesoproterozoic Grenville Orogeny, Neoproterozoic rifting, multiple phases of Paleozoic contractional deformation, and localized Mesozoic extension. Between southern Virginia and southern Pennsylvania, the Blue Ridge forms a NE-trending anticlinorium cored by Proterozoic basement. Along the flanks of the anticlinorium basement rocks are nonconformably overlain by the Lower Cambrian siliciclastic Chilhowee Group, which from bottom to top consists of the Weverton Formation, Harpers Formation, and the Antietam Formation. The anticlinorium developed above a NW-vergent thrust system during the Pennsylvanian-Permian Alleghanian Orogeny (e.g., Hatcher, 1989), although widespread greenschist-facies metamorphism and deformation within the basement initiated in the Late Devonian ( $\sim 360$  Ma) and continued until the early stages of Alleghanian shortening (e.g., Bailey et al., 2006). Cambrian and younger strata along the northwestern limb of the anticlinorium and adjacent Valley and Ridge Province record intense NW-vergent shortening but lack the pervasive metamorphism that characterizes the basement (e.g., Wickham, 1972; Southworth et al., 2009).

Several previous structural studies have documented deformation conditions within the Blue Ridge and Valley and Ridge province. NW-vergent, reverse-sense shear zones in Proterozoic Blue Ridge basement rocks record penetrative flattening strains and locally significant volume

loss ( $\sim 50$ – $60$ %) during late Paleozoic tectonism (Mitra, 1979; O'Hara, 1988; Bailey et al., 1994, 2007a). Mitra (1976, 1978) documented flattening strains within the Weverton Formation quartzite along the flanks of the Blue Ridge anticlinorium near the Virginia-Maryland border, with axial strain ratios approaching 7:1 along the northwestern, overturned limb of the anticlinorium. Regionally, dissolution-precipitation creep is the dominant deformation mechanism in the Chilhowee Group along the limbs of the anticlinorium, but dislocation creep is important in high strain zones along the northwest limb (Mitra, 1978, 1987), and in low strain samples rhomb-dominated quartz crystallographic preferred orientations may be produced by Dauphiné twinning (Rahl et al., 2018). In the Valley and Ridge province near the boundary with the Blue Ridge a gradational "tectonic front" separates quartzite that has undergone penetrative plastic strain to the east from quartzite that lacks appreciable penetrative strain and records primarily brittle deformation mechanisms west of the front (Fellows, 1943; Mitra, 1987). Grain-scale deformation of orthoquartzite/quartz arenite in the Valley and Ridge province has primarily occurred via cataclastic flow and extension fracturing (Mitra, 1987; Onasch et al., 2010).

## 3. Deformation of the Chilhowee Group near Front Royal, Virginia

### 3.1. Macroscale deformation

The western margin of the Blue Ridge in northern Virginia is bound by a SE-dipping thrust system that typically places Proterozoic basement rocks and Lower Cambrian Chilhowee Group strata over upper Cambrian to Ordovician strata. Near the town of Front Royal, the main frontal thrust fault splays into an E-W striking fault within the basement and the SE-dipping Happy Creek thrust fault that carries Antietam Formation quartzite in the hanging wall (Fig. 1, Wickham, 1972; Rader and Biggs, 1975; Lukert and Nuckols, 1976; Southworth et al., 2009). Our study area centers on the Antietam Formation exposed along the southern portion of the Happy Creek fault (Fig. 1). The Chilhowee Group in this area is folded into tight NE-trending anticlines and synclines with overturned northwest limbs and steeply SE-dipping axial surfaces (Figs. 2, 3). Pelitic intervals in the Harpers Formation record a SE-dipping axial planar cleavage (Figs. 2, 3a). Near the Happy Creek fault, the Antietam Formation is commonly brecciated. These brecciated zones are up to several hundred meters wide and vary from protocatclastic to crackle breccia in which bedding is still evident. Locally the Antietam Formation records a significant amount of penetrative strain, defining a foliation and stretching lineation (Figs. 4 and 5). Within this high strain zones *Skolithos* burrows in the Antietam Formation are stretched at a high angle to steeply-dipping bedding (Fig. 4). The thickness of the high strain zone is not well constrained due to limited exposure, but based on our cross-section analysis it is most likely between  $\sim 10$  m and 40 m thick (Fig. 2). Foliation in this high strain zone appears to be gently folded about a NE-plunging axis (Fig. 3b). This inferred fold axis has a similar orientation to the overall bedding fold axis, but the eigenvalues of poles indicate that the degree of foliation folding is less than that recorded by bedding. The G value, which quantifies the extent to which structural data define a girdle distribution compatible with folding about the minimum eigenvector (e.g., Vollmer, 1990), is 0.45 for poles to bedding and 0.28 for poles to foliation in the Antietam Formation. The presence of these fabrics at a high angle to bedding and evidence for gentle folding about a NE-plunging axis suggests that penetrative strain in the Antietam Formation developed during the late stages of folding along the western limb of the Blue Ridge. Penetrative strain appears to be concentrated near the stratigraphic base of the Antietam Formation, only locally extending into the brecciated zone (Figs. 2 and 6). This spatial pattern indicates that strain is not directly linked to the Happy Creek thrust fault.

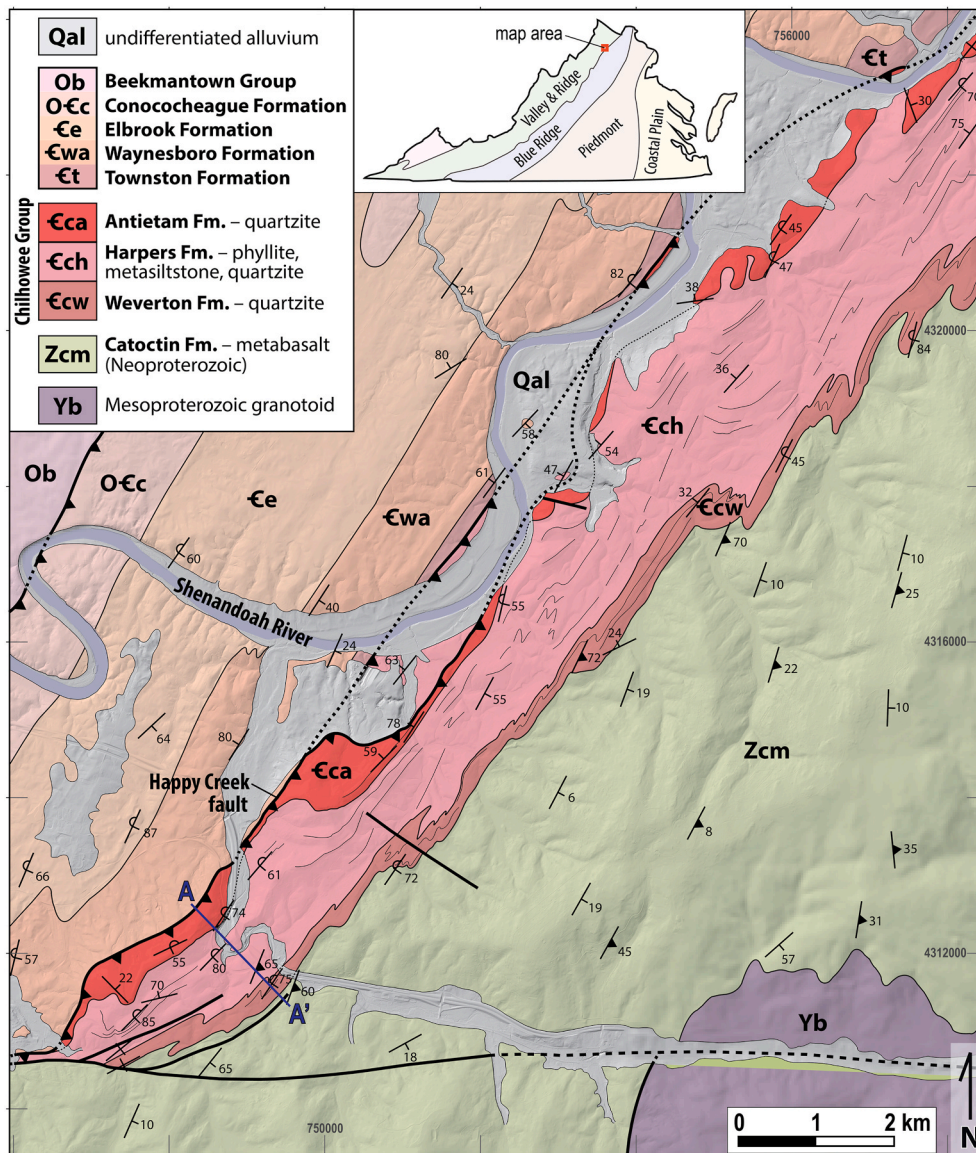


**Fig. 1.** Geologic map of the western margin of the Blue Ridge northeast of Front Royal, Virginia (based on mapping by Southworth et al. (2009), Lukert and Nuckols (1976), Rader and Biggs (1975), and Edmundson and Nunan (1973), with minor modifications from our fieldwork). The inset shows the major geological provinces in Virginia with the map area labelled in red. Coordinates along the margins of the map are in UTM WGS 84 format, and the hillshade background is from 1-m-resolution LiDAR data. Cross section A-A' is shown in Fig. 2. (For interpretation of the references to color in this figure legend, the reader is referred to the Web version of this article.)

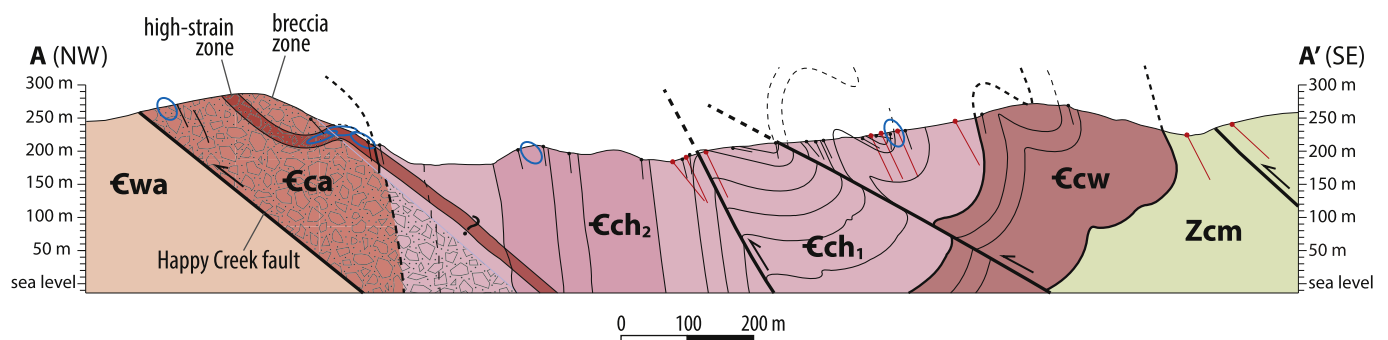


**Fig. 2.** Geologic cross section highlighting the deformation geometry of Chilhowee Group strata in the hanging wall of the Happy Creek thrust fault (based entirely on our mapping). See Fig. 1 for the cross-section location and unit explanation (CCh<sub>1</sub> is dominantly metasiltsone, whereas CCh<sub>2</sub> is metasandstone). The black and red lines at the surface show the apparent dip of bedding and cleavage, respectively, and the blue ellipses show the axial ratio along the section line from 3D strain analyses. (For interpretation of the references to color in this figure legend, the reader is referred to the Web version of this article.)

### 3.2. 3D strain geometry

To quantify the 3D strain magnitude and geometry of penetrative strain in the Chilhowee Group we used the  $R_f/\phi$  method (Ramsay, 1967;

Lisle, 1985) on oriented thin sections from 15 samples (12 Antietam Formation samples and 3 Harpers Formation samples). In all these samples the boundaries of detrital grains and/or detrital grains with optically continuous quartz overgrowths are clear and well suited for use

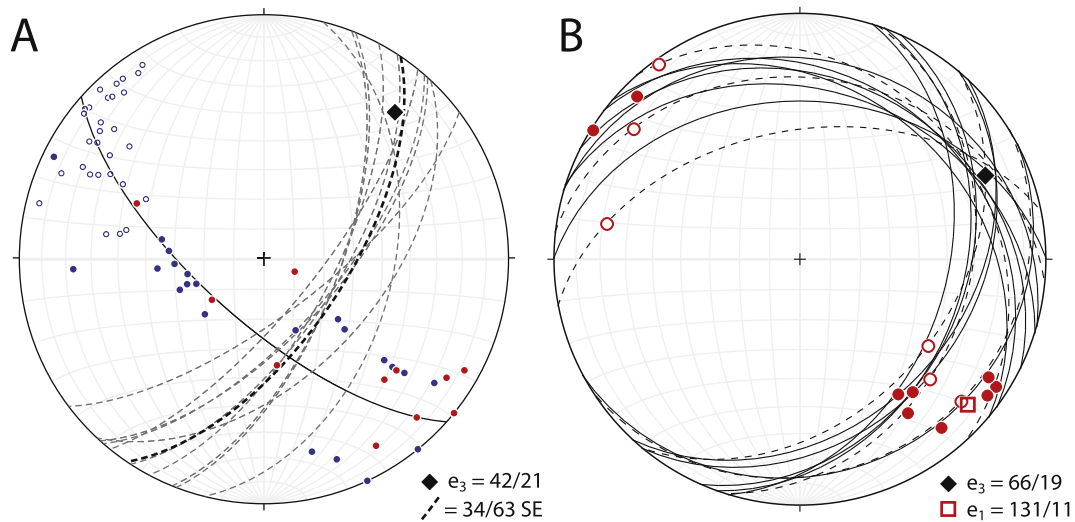


**Fig. 3.** Stereoplots of structural data from the Chilhowee Group in the area shown in Fig. 1. **A:** Poles to bedding (Weverton and Harpers Formation = blue; Antietam Formation = red; overturned beds are hollow) with a cylindrical best fit (solid great circle). The black diamond is the pole to the cylindrical best fit (minimum eigenvector, oriented 42/21). The dashed great circles are cleavage planes in the Harpers Formation (with the bold great circle representing the mean plane, oriented 34/63 SE). Point (P), Girdle (G), and Random (R) values from eigenvalues of poles to bedding are  $P = 0.436$ ,  $G = 0.448$ ,  $R = 0.116$ . Sources of bedding data:  $n = 47$  from this study,  $n = 17$  from Southworth et al. (2009) and  $n = 8$  from Edmundson and Nunan (1973). **B:** Moderate to high strain fabrics in the Antietam Formation (data from this study); solid great circles are foliation planes measured in outcrop; dashed great circles are foliation (X-Y) planes calculated from 3D strain analysis, and the black diamond is the minimum eigenvector of poles to all foliation planes (oriented 66/19), which we interpret as a fold axis. The red solid circles are stretching lineations measured in outcrop; the hollow red circles are X-axes calculated from 3D strain analyses, and the red square is the maximum eigenvector of all lineations/X-axes, oriented 131/11. For poles to foliation:  $P = 0.667$ ,  $G = 0.281$ ,  $R = 0.051$ . (For interpretation of the references to color in this figure legend, the reader is referred to the Web version of this article.)

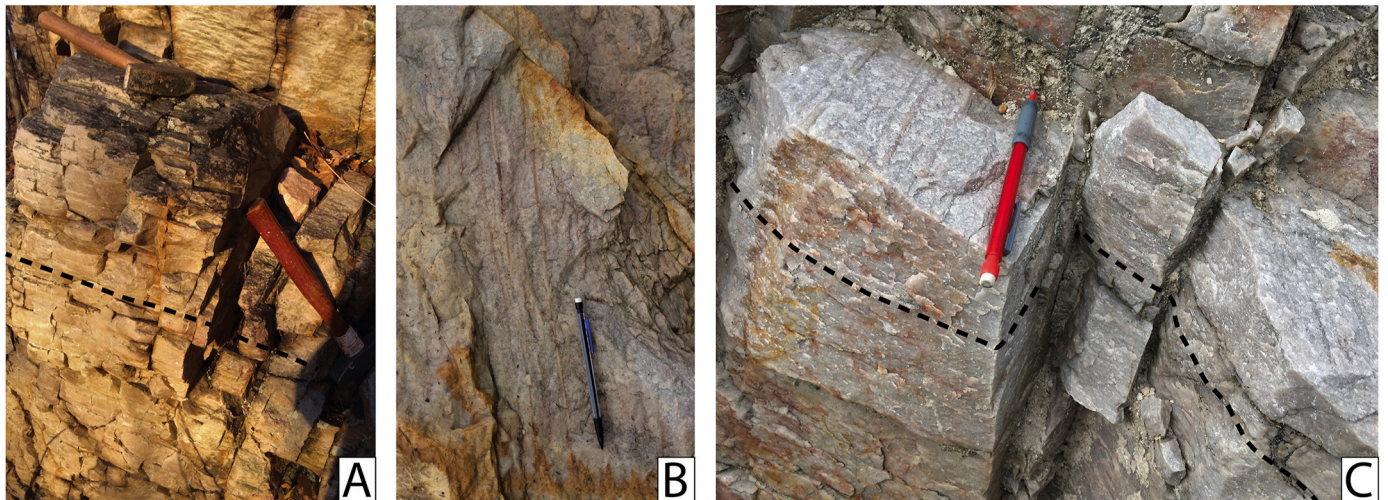


**Fig. 4.** Outcrop photographs of high-strain fabrics in the Antietam Formation. The black line in A and C parallels the trace of foliation, and the pencil in B and C parallels stretched *Skolithos* burrows. Foliation dips gently SE in A (sample 14-11-11 location), and the stretched *Skolithos* in B and C trend NE-SW and plunge shallowly (sample 14-11-6 location).

as strain markers, and the Antietam Formation is orthoquartzite with very little to no mica or detrital grains other than quartz. For each sample we cut 3 mutually perpendicular thin sections oriented with respect to bedding or, if evident, foliation. For each thin section >100 well-defined detrital quartz grains were traced from photomicrographs using Adobe Illustrator or the Adobe Draw app for tablets. Photomicrographs used for tracing were taken in plane-polarized light and cross-polarized light with the gypsum plate inserted in order to enhance identification of grain boundaries. Altogether we traced an average of

492 grains per sample to define the 3D strain geometry of the 15 samples, and we determined 2D strain from one additional sample (Fig. 7, Table 1, Supplementary Files 1, 2). Ellipses were fit to grain tracings using the software program SAPE (Mulchrone et al., 2005; 6 samples with names starting with 14) or EllipseFit (Vollmer, 2018; all 10 other samples; Table 1). All mean  $R$  and  $\phi$  values were calculated in EllipseFit using the shape matrix eigenvector method with an error calculated from bootstrap analysis of 1000 resamples (Shimamoto and Ikeda, 1976; Vollmer, 2018). In all sections the  $2\sigma$  error on the mean ellipse ratio ( $R$ )

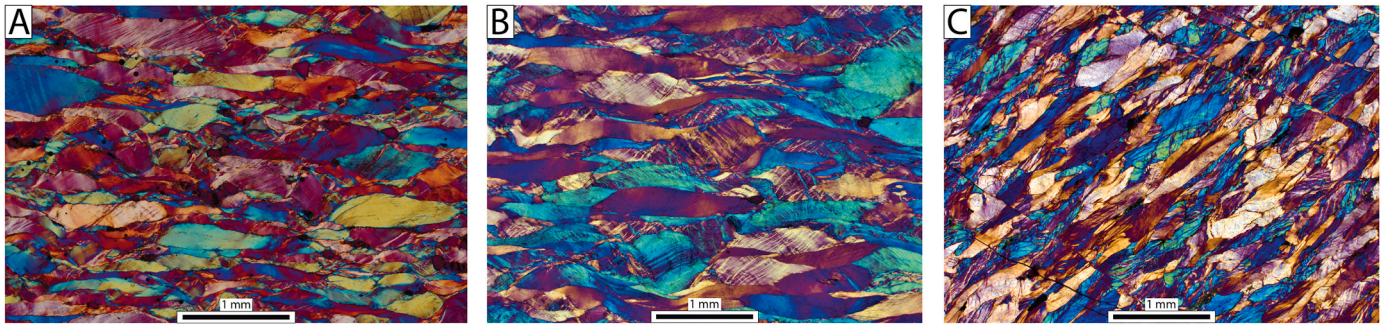


Fig. 5. Photomicrographs of high-strain Antietam Formation samples cut parallel to subparallel to the X:Z plane (cross-polarized light with gypsum plate). Detrital quartz grains are elongate parallel to the macroscopic foliation. A) sample 14-11-6, B) sample 150602-1, C) sample 150602-3. See Table 1 for sample coordinates and 3D strain data and Supplementary Files 1 and 2 for 2D strain data.

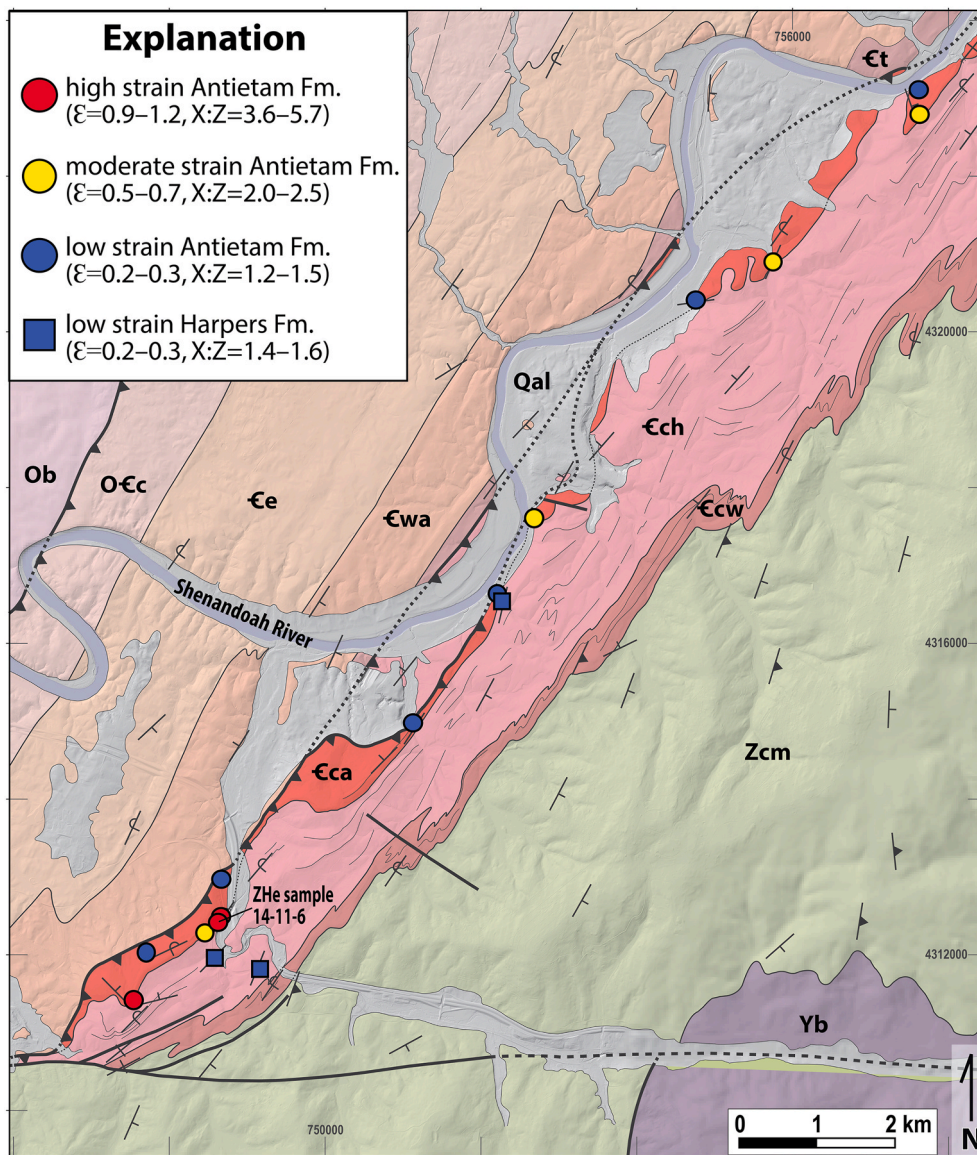
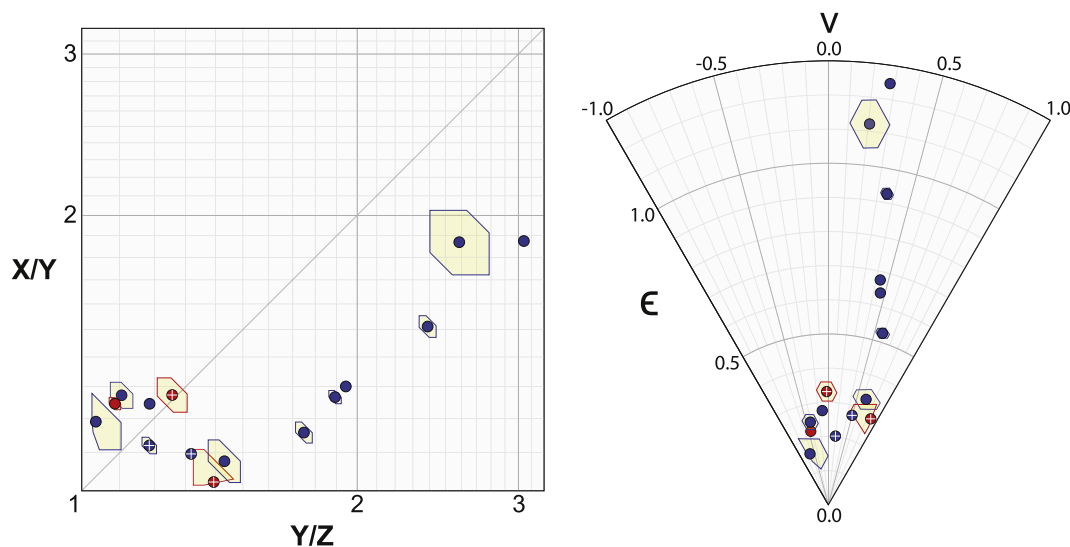


Fig. 6. Geologic map with location of samples analyzes for finite strain and zircon (U–Th)/He thermochronology (ZHe). The red and yellow samples are high strain and moderate strain Antietam Formation.  $\epsilon$  = octahedral shear strain. See Fig. 1 for unit explanation, bedding and foliation dip values, and sources of mapping. (For interpretation of the references to color in this figure legend, the reader is referred to the Web version of this article.)



**Fig. 7.** Flinn plot (left) and Nadai-Hsu plot (right) showing strain geometry from 3D strain analysis of Antietam Formation samples (blue) and Harpers Formation samples (red). The error boxes show the 95% confidence region. X, Y, and Z are the principal finite strain axes,  $\epsilon$  = octahedral shear strain, and V = Lode's ratio. The 4 samples with white crosses have stylolitic grain boundaries and/or dissolution seams. Strain analyses were carried out using Vollmer's computer program EllipseFit (Vollmer, 2018); see text for method details. (For interpretation of the references to color in this figure legend, the reader is referred to the Web version of this article.)

is 4–9%, with an average error of 5.3% (Supplementary File 1). On  $R_f/\phi$  plots moderate to high strain samples have well-defined normal distributions centered on the calculated  $\phi$  value (Supplementary File 2). All ellipsoids were calculated in EllipseFit using the Shan method (Shan, 2008) with errors based on bootstrap perturbation with 5000 resamples. In nearly all samples the ellipsoid errors are small (Table 1), defining a specific region on a Flinn and Hsu diagram (Fig. 7). Strain magnitudes are presented as octahedral shear strain ( $\epsilon$ ), where

$$\epsilon = \frac{1}{\sqrt{3}} \sqrt{(\ln S_x - \ln S_y)^2 + (\ln S_y - \ln S_z)^2 + (\ln S_z - \ln S_x)^2},$$

and  $S_x$ ,  $S_y$ , and  $S_z$  are the stretches along the principal finite strain axes (X, Y, Z).

Strain analyses indicate that the Antietam Formation locally records significant penetrative strain, with calculated X:Z ratios up to 5.7:1 and  $\epsilon$  values up to 1.25. The 6 highest strain samples with  $\epsilon > 0.5$  all record oblate strain geometries (general flattening; Flinn  $k$ -values = 0.21–0.55; Lode's ratio values = 0.21–0.59) with ~34–61% shortening along the Z-axis and ~33–120% elongation along the X-axis (Table 1). The calculated strain axis orientations match macroscopic foliation and lineation measurements, with N- to SE-dipping X-Y planes and X-axes that plunge NW or SE (Supplementary File 3). The remaining oriented samples, including all 3 Harpers Formation samples, record relatively little penetrative strain ( $\epsilon = 0.16$ –0.33, X:Z = 1.2–1.6) and variable strain geometries (Fig. 7, Table 1). One Harpers Formation very fine-grained metasandstone sample records a nearly perfect oblate strain ellipsoid ( $k = 0.06$ ) oriented parallel to SE-dipping axial planar cleavage observed at the outcrop, and the other two Harpers Formation samples also record E- to SE-dipping X-Y planes similar to cleavage orientations observed in the area (Supplementary File 3). Most of the calculated strain axis orientations in the low-strain Antietam Formation samples are generally compatible with either fabrics in the Antietam high-strain zone or cleavage in the Harpers Formation (Supplementary File 3).

### 3.3. Microscale deformation

Microstructures indicative of intracrystalline plastic strain are abundant in the Antietam Formation. Sweeping extinction, deformation lamellae, and extinction bands in quartz grains are common, even in low

strain samples. In high strain samples most grains have deformation lamellae, which are typically spaced ~2.5–4  $\mu\text{m}$  apart and oriented  $\leq 45^\circ$  from grain long axes (Fig. 8A–C). Deformation lamellae are commonly decorated with fluid inclusions. In addition, fluid-inclusion planes are pervasive in all Antietam samples, commonly transecting grain boundaries (Fig. 8C and D). The association of fluid inclusions with deformation lamellae and the continuation of fluid inclusion planes across grain boundaries indicates that fluids responsible for the inclusions were associated with quartzite deformation (rather than being inherited from the sedimentary source).

Minor zones of dynamically recrystallized quartz are locally present along grain margins and extinction bands in the Antietam Formation (Fig. 8D–F). These zones of dynamic recrystallization are more common in the higher strain samples, although we observed them in all but the 4 lowest strain Antietam samples, and recrystallized grains comprise  $\leq 1\%$  area in all samples. Recrystallized grains are consistently small ( $< 10 \mu\text{m}$ ) and commonly irregular in shape and dimension (Fig. 8D and E). Where present dynamic recrystallization is usually incomplete, with subgrains and sutured boundaries of larger grains typically present along with recrystallized grains. The relatively low amount of dynamic recrystallization, small grain size, and association of recrystallized grains with grain boundary bulges similar in size indicate that bulge nucleation was an important dynamic recrystallization process. Recrystallized grains are also associated with subgrains similar in size, indicating that subgrain rotation also played a role in dynamic recrystallization.

The three highest strain Antietam samples ( $\epsilon = 0.93$ –1.25; Table 1) record evidence of brittle-plastic strain. Discrete extinction bands that resemble both wide extinction bands and localized extinction bands according to the Derez et al. (2015) classification scheme are common in these samples (Fig. 8F). Many of these bands record bulging and apparent minor dynamic recrystallization, although similar granular textures associated with localized extinction bands have been interpreted to record fracturing modified by solution-precipitation processes (Derez et al., 2015). Most localized extinction bands are oriented  $< 60^\circ$  from the grain long axes, and commonly record micron-scale opening perpendicular to the bands or normal-sense shear offset of older extinction bands and/or grain boundaries (Fig. 8F). In oriented X-Z thin sections these normal-sense offsets are both top-SW and top-NE, and

**Table 1**  
 Sample information and 3D strain data. Sample coordinates are in UTM (Universal Transverse Mercator) WGS 84, zone 17.  $S_x$ ,  $S_y$ , and  $S_z$  = calculated stretch along the principal finite strain axes (X, Y, Z). All samples except 150602-3 and DrByc-650 are oriented. Ellipsoids were calculated using the Shan method (Shan, 2008) in EllipseFit (Vollmer, 2018); errors were calculated using bootstrap perturbation with sigma 3.0 and 5000 resamples (default EllipseFit settings); rms = root mean square measure of the variation of the residuals from the ellipse; dist = distance; k-value = Fimm's k-value =  $(\frac{X}{Y}-1)/(\frac{X}{Z}-1)$ ;  $\nu$  = Lode's parameter =  $(2 \ln S_y - \ln S_x - \ln S_z)/(\ln S_x - \ln S_z)$ ;  $\epsilon$  = octahedral shear strain =  $\frac{1}{\sqrt{3}} \sqrt{(\ln S_x - \ln S_y)^2 + (\ln S_y - \ln S_z)^2 + (\ln S_x - \ln S_z)^2}$ . See Supplementary Files 1 and 2 for 2D strain data.

Sample	Formation	UTM_E	UTM_N	$S_x$	trend	plunge	$S_y$	trend	plunge	$S_z$	trend	plunge	R rms	$\phi$ rms	dist.rms	X/Y	Y/Z	X/Z	k-value	$\nu$ (Lode's)	$\epsilon$ (strain)
150602-3	Antietam	747544	4311417	2.20	-	-	1.18	-	-	0.39	-	-	0.00	0.0	0.00	1.87	3.04	5.70	0.43	0.28	1.25
150602-1	Antietam	748666	4312488	2.08	280.5	21.3	1.11	29.0	39.1	0.43	169.0	43.3	0.22	0.3	0.07	1.87	2.59	4.83	0.55	0.21	1.12
14-11-6	Antietam	748629	4312415	1.76	324.1	2.5	1.16	55.1	23.2	0.49	228.3	66.6	0.05	0.4	0.02	1.51	2.39	3.61	0.37	0.36	0.93
14-11-11	Antietam	752684	4317606	1.49	131.4	14.1	1.14	222.5	4.0	0.59	328.1	75.3	0.01	0.1	0.01	1.30	1.94	2.53	0.32	0.43	0.68
150602-2	Antietam	748459	4312279	1.45	132.7	29.2	1.14	36.5	10.9	0.60	288.2	58.5	0.03	0.2	0.02	1.27	1.89	2.39	0.30	0.46	0.64
15-6-8	Antietam	755750	4320897	1.33	308.1	15.2	1.15	44.4	22.0	0.66	186.2	62.9	0.03	2.1	0.04	1.16	1.75	2.02	0.21	0.59	0.53
14-9-2	Harpers	752272	4316538	1.27	142.2	30.0	1.00	30.3	32.9	0.79	264.0	42.5	0.05	2.3	0.04	1.27	1.26	1.60	1.06	-0.03	0.33
15-6-5	Antietam	751130	4314977	1.18	124.0	37.5	1.10	216.3	3.0	0.77	310.1	52.3	0.04	6.8	0.04	1.08	1.43	1.54	0.18	0.66	0.33
14-11-7	Harpers	749166	4311817	1.13	146.3	65.6	1.11	42.1	6.4	0.80	309.3	23.5	0.03	9.2	0.03	1.02	1.39	1.42	0.06	0.88	0.28
15-6-4	Antietam	747707	4312029	1.22	197.2	0.3	0.98	288.0	72.8	0.83	107.1	17.2	0.01	0.3	0.01	1.22	1.19	1.48	1.31	-0.12	0.28
14-11-9	Antietam	748669	4312968	1.17	44.2	61.0	1.06	168.3	17.3	0.81	265.8	22.5	0.01	0.5	0.01	1.10	1.32	1.44	0.31	0.50	0.27
15-6-7	Antietam	754758	4320407	1.21	315.3	10.9	0.95	54.2	38.7	0.86	212.3	49.2	0.03	3.8	0.04	1.27	1.11	1.40	2.57	-0.41	0.25
14-11-5	Harpers	748586	4311958	1.19	81.1	18.2	0.96	190.6	45.5	0.88	335.7	38.8	0.02	2.5	0.02	1.25	1.09	1.35	2.81	-0.45	0.22
15-4-1	Antietam	757620	4323108	1.14	31.5	25.9	1.02	136.8	28.5	0.86	266.6	49.7	0.03	2.3	0.02	1.12	1.19	1.33	0.65	0.20	0.20
15-6-6	Antietam	752211	4316636	1.14	115.0	53.6	0.96	257.1	30.2	0.92	358.2	18.4	0.04	14.9	0.07	1.19	1.04	1.23	5.25	-0.66	0.16
DrByc (2D)	Antietam	757630	4322791	1.4	-	-	1.0	-	-	0.7	-	-	-	-	-	1.4	1.4	2.0	-	-	$\geq 0.5$

overall there is no clear dominant sense of shear. Extinction bands associated with shear are typically ~3–20  $\mu\text{m}$  wide, but locally they thin into discrete fractures. Shear fractures, localized extinction bands, and cataclastic zones 100s of  $\mu\text{m}$  thick are abundant in the highest strain sample (150602-3), where they commonly transect the entire thin section (Fig. 8G). Extinction bands within grains locally have a fibrous quartz habit overprinted by subgrain development and minor bulging recrystallization, suggesting at least some of these bands originated as veins (Fig. 8H). Cathodoluminescence (CL) is likely needed to understand brittle processes responsible for formation of the fluid-inclusion planes and extinction bands (e.g., Milliken and Laubach, 2000; Anders et al., 2014).

In most Antietam Formation samples thin ( $\leq 100 \mu\text{m}$ ) quartz rims are present along a small percentage of grain margins. These rims are typically fibrous and commonly contain trace amounts of very fine (~3–30  $\mu\text{m}$  long) mica, suggesting they precipitated as fringes during dissolution-precipitation creep. Compared to the detrital grains, these rims preferentially record subgrain development and minor bulging + subgrain rotation recrystallization (Fig. 8H). Sutured or indented grain boundaries that likely record dissolution (pressure solution) are present in all samples, although consistently irregular and/or stylolitic grain boundaries are only common in two low strain Antietam samples ( $\epsilon \leq 0.27$ ; samples 14-11-9 and 15-4-1; Table 1; Fig. 8I). Minor subgrain development and bulging are locally present along sutured grain boundaries.

### 3.4. Quartz dynamically recrystallized grain size and piezometry

We estimated quartz dynamically recrystallized grain sizes for 9 Antietam Formation samples by tracing >200 recrystallized grains per sample on photomicrographs of the highest strain sections, converting grain area to an equivalent circular diameter. The root mean square (RMS) grain size ranges from 3.3  $\mu\text{m}$  to 7.1  $\mu\text{m}$ . Most samples record RMS grain sizes ~4–5  $\mu\text{m}$ , and the average RMS grain size for all 9 samples is  $4.8 \pm 1.1 \mu\text{m}$  ( $\pm 1\sigma$  standard deviation; Fig. 9). The 3 highest strain samples (with  $\epsilon = 0.93$ –1.25) record an average RMS grain size of  $3.8 \pm 0.5 \mu\text{m}$  (Fig. 9). In all samples the RMS grain size is 0.1–0.6  $\mu\text{m}$  greater than the arithmetic mean, geometric mean, and median grain size. The range of grain sizes in any given sample is narrow, with a mean standard deviation of ~1.2  $\mu\text{m}$  (Fig. 9).

Dynamically recrystallized grain size is a function of differential stress during recrystallization and appears to be independent of temperature, strain rate, or water content (e.g., Mercier et al., 1977; Twiss, 1977; Stipp and Tullis, 2003; Stipp et al., 2006). In addition, grain sizes associated with very minor magnitudes of bulging recrystallization appear to faithfully record differential stress, suggesting formation of a steady-state fabric is not needed for application of the quartz piezometer (Kidder et al., 2012). Most rheologic studies of quartz deformation use the experimentally calibrated recrystallized grain size piezometer of Stipp and Tullis (2003). A calibration correction to this piezometer proposed by Holyoke and Kronenberg (2010) shifts stress magnitudes down ~27%. Over the past 10 years this correction has been inconsistently applied, and the accuracy of quartz piezometry is unclear. Application of the Stipp and Tullis (2003) piezometer to the Antietam samples yields differential stress magnitudes ranging from 141 MPa to 259 MPa, with a mean of 200 MPa, or 103 MPa to 190 MPa with a mean of 146 MPa with the Holyoke and Kronenberg (2010) correction (Fig. 9). Higher stresses indicated by the uncorrected Stipp and Tullis (2003) piezometer are more consistent with the presence of deformation lamellae, which Blenkinsop and Drury (1988) interpret to form at differential stresses of at least 170 MPa. In addition, the deformation lamellae spacing of  $\leq 4 \mu\text{m}$  in the Antietam Formation suggests differential stresses of  $\geq 178 \text{ MPa}$  based on the quartz deformation lamellae spacing piezometer calibrated in experiments by Koch and Christie (1981).

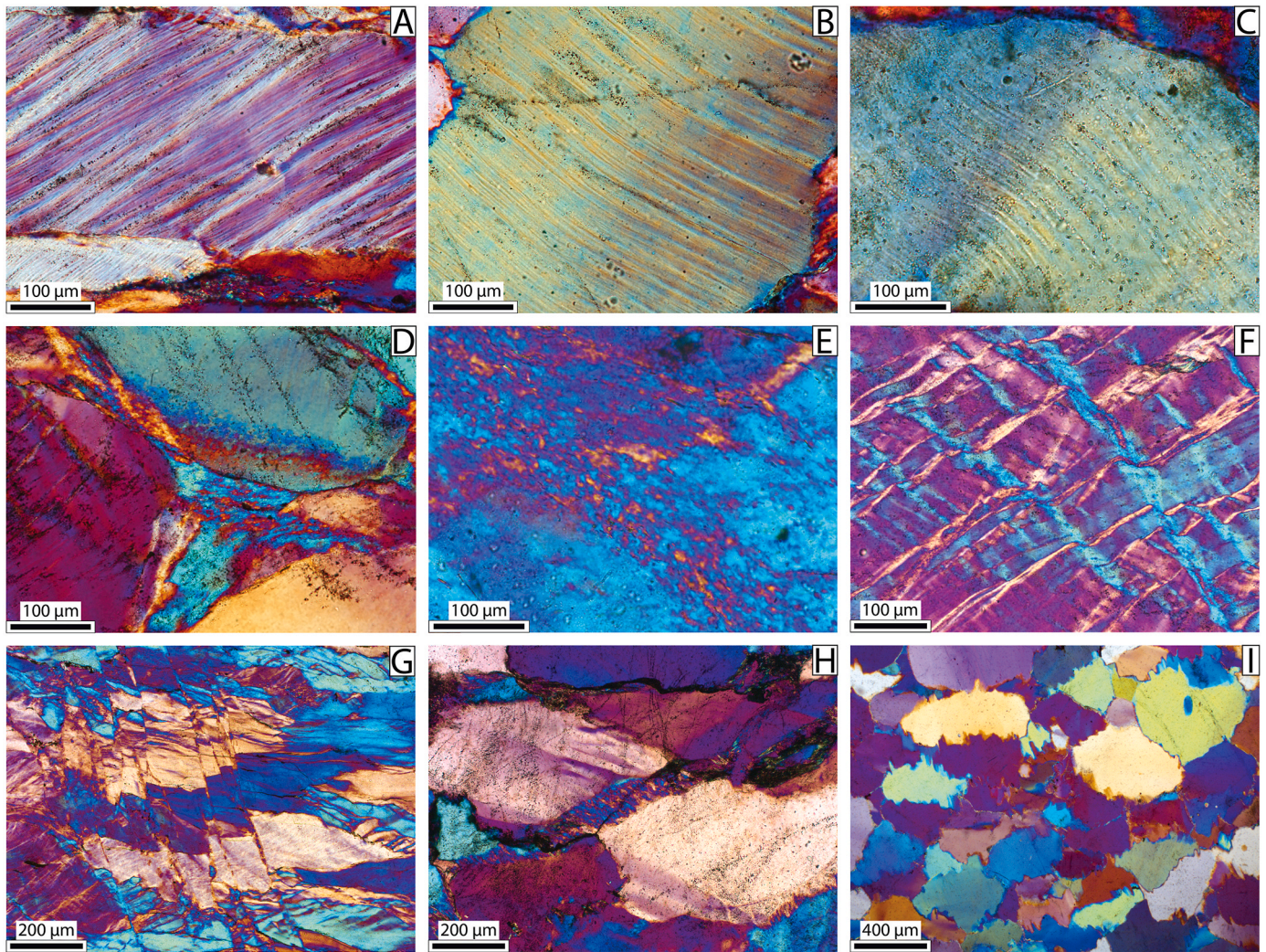


**Fig. 8.** Photomicrographs of Antietam Formation samples in cross-polarized light with gypsum plate inserted. A), B), and C) Deformation lamellae and parallel trails of fluid inclusions (in samples 14-11-6, 14-11-11 and 150602-1, respectively). D) Minor quartz dynamic recrystallization and subgrain development along grain margins (sample 14-11-11); E) Quartz dynamic recrystallization and subgrain development (sample 150602-3); F) Extinction bands locally associated with shear displacement, bulging, and subgrain development; sample 150602-1); G) Shear fractures with minor quartz subgrain development and bulging (sample 150602-3); H) Example of fibrous quartz vein fill (center) and fringe (bottom right) that has undergone subgrain development and minor dynamic recrystallization (sample 15-6-8); I) Stylolitic grain boundaries formed by dissolution (sample 15-4-1).

### 3.5. Quartz crystallographic fabrics

#### 3.5.1. EBSD methods

We studied 6 Antietam Formation samples using electron backscatter diffraction (EBSD) to characterize the crystallographic preferred orientations (CPOs) of quartz. Analyses were performed on standard polished thin-sections, each treated with a final chemical-mechanical polishing step using a colloidal silica slurry. We used a Zeiss EVO MA 15, Scanning Electron Microscope (SEM) at Washington and Lee University with an Oxford Instruments EBSD detector and Aztec software. Operating conditions included an accelerating voltage of 25 kV, a probe current of 20–25 nA, and a working distance between 15 and 25 mm. To avoid charging issues, the SEM operated in low-vacuum with a pressure of 30 Pa.

For samples 14-11-6 and 14-11-11 EBSD data were collected along an x-y grid on a series of non-overlapping maps ( $375 \times 500 \mu\text{m}$ ) at a step size of 30–50  $\mu\text{m}$ . For all other samples, the data were collected at a step size of 4–25  $\mu\text{m}$  using the Large Area Mapping feature in Aztec, with points collected on individual maps ( $300 \times 400 \mu\text{m}$ ) that were then merged together into a single large map within Aztec. In all samples these EBSD maps covered a sufficiently large enough area and number of

detrital grains (>600) to sufficiently characterize the bulk CPO. The EBSD data were processed and analyzed using the MTEX toolbox for Matlab (Hielscher and Schaeben, 2008). Low-quality data with mean angular deviation (M.A.D.) values > 1.0 were removed from the analysis. Given the large grain size relative to sampling step size (mean detrital grain diameter typically  $\sim 0.2\text{--}0.6 \text{ mm}$ ) and the relatively large total area covered by EBSD analyses, we present all the data points analyzed in the pole figures to best characterize the CPO within the sample volume. Fabric parameters were calculated in MTEX using algorithms from Mainprice et al. (2015), and we use the J-factor index (Bunge, 1982) and M-index (Skemer et al., 2005) to evaluate CPO strength.

All quartz pole figures are presented on lower hemisphere stereoplots in the finite strain X:Z reference frame with the southeast side of the X-axis on the right (Fig. 10). This reference frame was determined by 3D strain analyses, which yielded well-defined finite strain axis orientations (Table 1).

#### 3.5.2. Crystallographic fabrics

The 6 Antietam Formation samples analyzed for EBSD include 2 high strain samples ( $\epsilon = 0.9\text{--}1.1$ ; samples 150602-1 and 14-11-6), 3

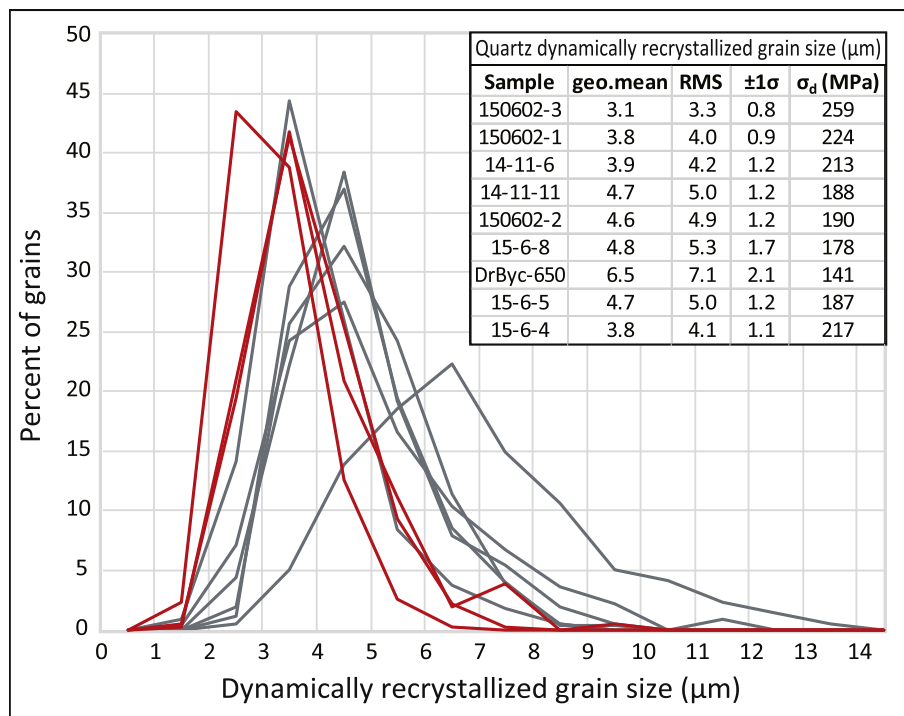


**Fig. 9.** Histogram and table of dynamically recrystallized grain sizes from 9 Antietam Formation samples. Grain sizes were determined by tracing 202 to 353 recrystallized grains per sample and converting area to an equivalent circular diameter. The histograms in red are the 3 highest strain samples (150602-3, 150602-1, and 14-11-6). geo.mean = geometric mean grain size; RMS = root mean square grain size;  $\sigma_d$  = differential stress based on the [Stipp and Tullis \(2003\)](#) grain size piezometer. (For interpretation of the references to color in this figure legend, the reader is referred to the Web version of this article.)

moderate strain samples ( $\mathcal{E} = 0.5\text{--}0.7$ ; samples 14-11-11, 150602-2, and 15-6-8), and 1 low-strain sample ( $\mathcal{E} = 0.3$ ; sample 15-6-5) ([Fig. 10](#), [Table 2](#)). All samples have moderate to well-defined quartz CPOs with a J-factor index  $>1.5$ , including sample 15-6-5 with a mean X:Z of only 1.54. CPO strength generally correlates with strain, but all samples have similar patterns. C-axes cluster around the Z-axis, whereas a-axes form broad, weakly-defined girdles subparallel to the X-Y (foliation) plane ([Fig. 10](#)). In some samples (e.g., 14-11-11) the concentration of c-axes form two point maxima centered on the Z-axis, whereas in other samples (e.g., 150602-1) the c-axes appear to be clustered in one point maxima near the Z-axis ([Fig. 10](#)). The single point maxima distributions resemble c-axis patterns in quartzite deformed experimentally by [Tullis et al. \(1973\)](#) at relatively low-temperature and/or high strain rates under uniaxial flattening conditions. In the 4 highest strain Antietam samples the c-axes maxima are connected by a weakly defined girdle, whereas the a-axes are slightly more concentrated near the X-axis ([Fig. 10](#)). CPO fabrics in these 4 samples are symmetric about the finite strain axes, suggesting coaxial-dominated strain. Sample 15-6-8 is the only one with clear asymmetry. The c-axis maxima and the a-axis girdle in 15-6-8 are counterclockwise of the Z-axis and X-Y plane, respectively, suggesting a component of top-NW shear ([Fig. 10](#)).

The CPO patterns in the Antietam samples resemble quartz fabrics predicted to form during general flattening strain (associated with oblate triaxial strain ellipsoids). That is, the fabrics are intermediate between uniaxial flattening (with small-circle c-axis girdles around the Z-axis and two a-axis great circle girdles at a low angle to the X-Y plane) and plane strain (with a c-axis type 1 crossed girdle and 4 a-axis maxima near the X-axis) ([Lister and Hobbs, 1980](#); [Schmid and Casey, 1986](#)). This strain geometry inferred from CPOs is consistent with the 3D strain analyses of these samples, which indicate a general flattening strain with Flinn k-values  $\sim 0.2\text{--}0.5$  ([Table 1](#)).

#### 4. Deformation conditions and rheology of penetrative strain in the Antietam Formation

##### 4.1. Deformation mechanisms

Microstructures in the Antietam Formation provide insight into quartz deformation mechanisms. In the high strain Antietam samples, abundant deformation lamellae, minor zones of dynamic recrystallization, and the presence of a well-defined crystallographic preferred orientation clearly indicate that dislocation creep was important during penetrative deformation. Quartz deformation lamellae are common in rocks that have undergone relatively low-temperature dislocation creep, where they usually represent dislocation tangles or subgrain walls (e.g., [White, 1973](#); [Blenkinsop and Drury, 1988](#); [Drury, 1993](#); [Trepmann and Stöckhert, 2003](#)). The orientations of deformation lamellae in a sample of high strain Antietam Formation (from a location near samples 14-11-6 and 150602-1) were studied by [Wickham \(1972\)](#), who demonstrated that lamellae were most commonly oriented  $5\text{--}25^\circ$  from basal planes (with  $\sim 95\%$  oriented  $<45^\circ$ ). Quartz basal planes have a preferred orientation subparallel to foliation, consistent with lattice reorientation dominantly via basal  $\langle a \rangle$  slip.

The 3 highest strain Antietam samples also record minor brittle deformation in the form of intragranular quartz veins and extinction bands/discrete fractures with shear displacement. These structures helped accommodate grain elongation, and the apparent lack of a preferred vein or shear fracture orientation suggests they contributed to an overall coaxial strain, consistent with the CPO symmetry. Bulging, subgrain development, and minor recrystallization are preferentially developed along these structures, indicating dislocation creep and brittle strain were coeval. The Antietam Formation high strain zone thus records coaxial strain at or near the brittle-plastic transition.

The presence of sutured grain boundaries and fibrous quartz fringes along some grains point to dissolution-precipitation creep as another deformation mechanism in the Antietam Formation. Quantifying the strain contribution from dislocation creep vs. dissolution-precipitation creep is difficult (e.g., [Mitra, 1976](#)). Although sutured or indented

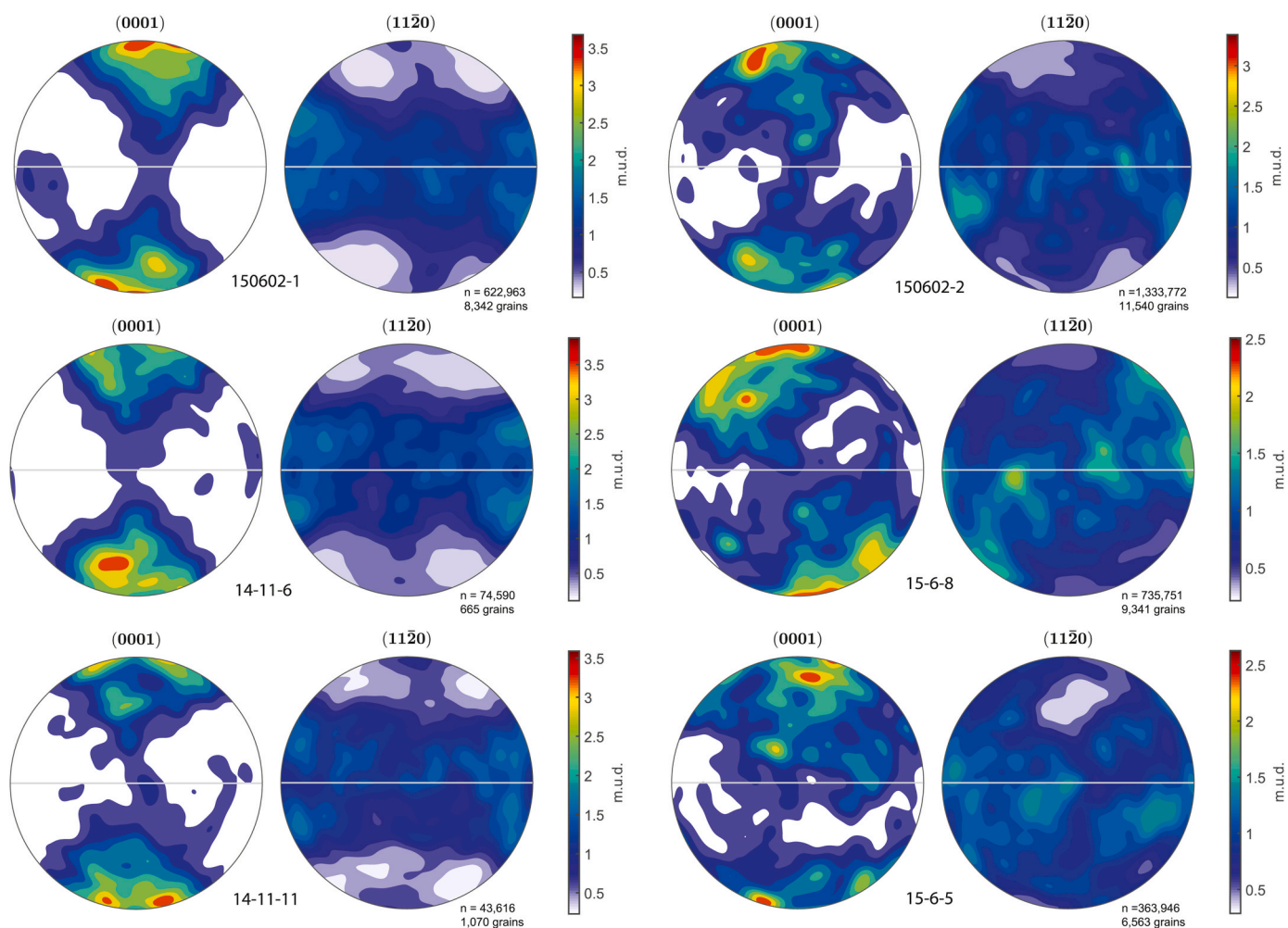


**Fig. 10.** Lower-hemisphere pole figures of quartz  $c$ -axes (0001) and  $a$ -axes ( $11\bar{2}0$ ) from EBSD analysis of 6 Antietam Formation samples (arranged from highest strain in the top left to lowest strain in the bottom right). All pole figures are presented in the X-Z reference frame with the southeast side of the X-axis on the right.  $n$  = the number of data points; the number of grains is based on a minimum of 4 points per grain; m.u.d. = multiples of uniform distribution contour interval. EBSD data were processed and analyzed using the MTEX toolbox for Matlab (Hielscher and Schaeben, 2008).

**Table 2**

EBSD data and  $c$ -axis opening angle values from Antietam Formation samples. Fabric parameters were calculated in MTEX using algorithms from Mainprice et al. (2015); J-factor (Bunge, 1982) and M-index (Skemer et al., 2005) are measures of crystallographic preferred orientation strength; P, G, and R values are based on eigenvalues of  $c$ -axes and quantify the extent to which data form a point-maxima (P), girdle (G), or random (R) distribution (Vollmer, 1990); OA = opening angle in degrees.  $c$ -axis OA values at  $10^\circ$  and  $5^\circ$  half-widths are from the automated symmetry analysis method of Hunter et al. (2018), and the temperature is based on the mean  $c$ -axis opening angle using the calibration of Faleiros et al. (2016) and uncertainty interpreted to be at least  $\pm 50^\circ\text{C}$ .

SAMPLE	$\nu$ (Lode's parameter)	$\epsilon$ (octahedral shear strain)	J-factor	M-index	P	G	R	$c$ -axis OA (manual estimate)	$c$ -axis OA ( $10^\circ$ half-width)	$c$ -axis OA ( $5^\circ$ half-width)	$c$ -axis OA (mean)	Temperature $\pm$ error ( $^\circ\text{C}$ )
150602-1	0.21	1.12	2.280	0.102	0.35	0.09	0.56	no solution	no solution	no solution	no solution	no solution
14-11-6	0.36	0.93	3.251	0.177	0.45	0.15	0.40	$32 \pm 1$	24.5	33.5	30.0	$255 \pm 50$
14-11-11	0.43	0.68	2.304	0.090	0.33	0.12	0.55	$29 \pm 1$	29	27.5	28.5	$245 \pm 50$
150602-2	0.46	0.64	1.508	0.043	0.20	0.14	0.66	$38 \pm 2$	36	34.5	36.2	$298 \pm 50$
15-6-8	0.59	0.53	1.508	0.032	0.21	0.02	0.77	$33 \pm 3$	30.5	27.5	30.3	$257 \pm 50$
15-6-5	0.66	0.33	1.519	0.028	0.17	0.08	0.75	$48 \pm 1$	50.5	48.5	49.0	$386 \pm 50$

grain boundaries that likely record dissolution are common, stylonitic grain boundaries that clearly record pervasive dissolution are only widespread in two low strain samples (15-4-1 and 14-11-9). Dissolution-precipitation creep is frequently associated with volume loss, particularly in argillaceous rocks but also in quartzofeldspathic shear zones in the Blue Ridge (O'Hara, 1988; Newman and Mitra, 1993; Bailey et al., 1994, 2007a). Quartz-rich rocks lacking micas may also

experience true volume loss during dissolution-precipitation creep, as some component of dissolved quartz typically leaves the system at the sample scale (e.g., Mosher, 1987; Onasch, 1994). To evaluate potential volume loss in the Antietam Formation we used geochemical data from 10 samples with a range of strain values (Supplementary File 4). Volume loss should increase the relative concentration of immobile elements such as Zr, Al, and Ti (e.g., O'Hara, 1990) and may result in an apparent

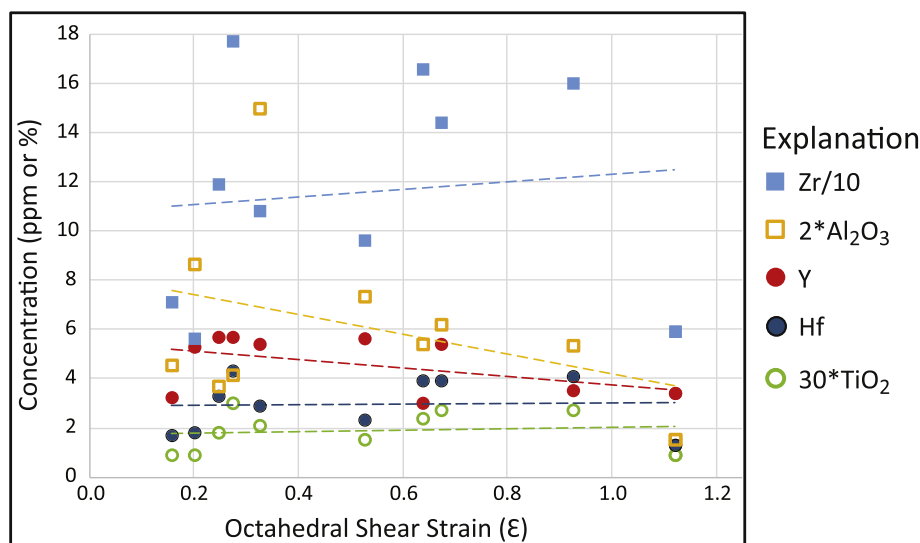


**Fig. 11.** Concentration of immobile elements (Zr, Al<sub>2</sub>O<sub>3</sub>, Y, Hf, and TiO<sub>2</sub>) vs. octahedral shear strain in 10 Antietam Formation samples. Geochemical analyses were performed at ALS Minerals in Reno, Nevada using x-ray fluorescence (XRF) inductively coupled plasma (ICP) atomic emission spectroscopy and ICP mass spectrometry with lithium borate fusion prior to acid dissolution. The dashed trendlines are linear regressions of the data. Overall the concentration of these elements does not increase with strain, suggesting volume loss due to dissolution-precipitation creep strain was not important.

flattening strain (e.g., Ramsay and Wood, 1973). There is no apparent correlation between strain and concentration of immobile elements in the Antietam Formation (Fig. 11). These data indicate that either volume loss via dissolution was insignificant or that the compositional heterogeneity of the Antietam Formation is too large to clearly detect volume changes. Flattening strains in the Antietam Formation are most likely unrelated to volume loss, as quartz CPOs in the moderate to high strain samples record flattening strain via lattice reorientation during dislocation creep (which does not involve volume change) (Fig. 10).

Regionally, dissolution-precipitation creep was likely dominant along the flanks of the Blue Ridge (Mitra, 1987), including within some high strain zones in the Chilhowee Group (Mitra, 1978). However, Mitra (1987) noted that the proportion of dislocation creep to dissolution-precipitation creep strain is higher along the overturned, western limb of the Blue Ridge anticlinorium. Mitra (1987) determined 2D stretches of 1.8 and 2.1 in two Antietam samples from the high strain zone near Front Royal using deformed rutile needles within elongate quartz grains, which may provide good estimates of intracrystalline finite strain due to dislocation creep (Mitra, 1976; Mitra and Tullis, 1979). These strain values match those we determined in our 3D strain analyses of the highest strain samples from the same area ( $S_x = 1.8-2.2$ ; Table 1). Our strain analyses are based on grain shapes and thus do not distinguish between dislocation creep strain vs. dissolution-precipitation creep strain. The similarity between these strain values and the strain values from intragranular rutile deformation (Mitra, 1987) strongly suggest that the vast majority of strain was accommodated by dislocation creep.

**Table 3**

FTIR water content data for Antietam Formation samples. strain ( $\epsilon$ ) = octahedral shear strain from 3D strain analyses; # sites analyzed = number of water content analysis sites per sample; stdev = 1 $\sigma$  standard deviation of water content values; RMS = root mean square of water content values.

Sample	strain ( $\epsilon$ )	# sites analyzed	Water content (ppm)*				
			range	median	mean	stdev	RMS
15-6-6	0.16	100	6-989	149	224	211	306
14-11-9	0.27	100	61-1,768	428	498	332	598
150602-2	0.64	100	7-1,054	111	164	180	243
14-11-11	0.68	170	33-2,265	285	401	366	542
14-11-6	0.93	87	37-1,346	205	296	271	400
150602-1	1.12	110	29-1,222	163	226	192	296
150602-3	1.25	100	35-388	218	215	72	226

\*ppm=(H:10<sup>6</sup> Si)/6.67

Based on the microstructural observations and data outlined above, we interpret quartz dislocation creep to have been the dominant deformation mechanism in the Antietam Formation high-strain zone, with basal  $\langle a \rangle$  glide accommodating the majority of penetrative strain. Dissolution-precipitation creep was locally important in the Antietam Formation, but dislocation creep is primarily responsible for development of the Antietam high strain zone near Front Royal.

#### 4.2. Quartzite water content and hydrolytic weakening

##### 4.2.1. FTIR spectroscopy

The abundance of fluid-inclusion planes and deformation lamellae decorated with fluid inclusions suggest fluids played an important role in deformation of the Antietam Formation. Intragranular water may enhance crystal plasticity and significantly lower the strength of quartz during dislocation creep, an effect known as hydrolytic weakening (e.g., Griggs, 1967; Blacic, 1975; Hirth and Tullis, 1992). Numerous studies have investigated the deformation conditions and rheology of quartz during dislocation creep, but relatively few studies have quantified quartz intragranular water content in naturally-deformed tectonites. To evaluate the possible influence of hydrolytic weakening during penetrative strain of the Antietam Formation, we determined water content in 7 samples using Fourier Transform Infrared (FTIR) spectroscopy.

FTIR spectroscopy analyses were performed on doubly-polished thick sections from 7 Antietam Formation samples – 3 high strain samples (150602-3, 150602-1, 14-11-6), 2 moderate strain samples (150602-2, 14-11-11), and 2 low strain samples (14-11-9, 15-6-6;

**Table 3;** Supplementary File 5). The thick sections were removed from glass slides and cleaned in baths of acetone and ethanol, resulting in doubly-polished wafers of quartzite ~100 μm thick. The vast majority of individual quartz crystals in these samples range from ~200 to 700 μm in equivalent spherical diameter. In most positions the wafer width is less than this crystal size, creating clear optical pathways that are not complicated by internal grain boundaries. We used FTIR spectroscopy to determine the dissolved H<sub>2</sub>O content in quartz crystals. FTIR spectra were collected using a ThermoElectron Nicolet iN10 infrared microscope and spectrometer operating in mid-IR, from 500 to 4000 cm<sup>-1</sup> with 64 scans and a spectral resolution of 4 cm<sup>-1</sup>. Reported H<sub>2</sub>O contents in quartz are determined from the broad absorbance at ~3400 cm<sup>-1</sup>, specifically measured as the integrated area of the absorbance peak above a linear baseline between ~2900 and 3700 cm<sup>-1</sup> (Supplementary File 6). Absorbances were converted to molar ppm H<sub>2</sub>O (H:10<sup>6</sup> Si) using a modified Beer-Lambert Law following the calibration of **Kats**

(1962):  $C = (0.812 \times A_i)/t$ , where C is H:10<sup>6</sup> Si, A<sub>i</sub> is the integrated absorbance (cm<sup>-1</sup>), and t is sample thickness (cm). Following **Gleason and DeSisto (2008)**, we report water content as ppm H<sub>2</sub>O by weight, which is equal to (H:10<sup>6</sup> Si)/6.67.

At the exact location of each FTIR analysis we measured section thickness optically by focusing on the top and bottom surface of the wafer using a petrographic microscope with a Heidenhain linear encoder that measures stage height. Uncertainties in thickness ranged up to ~10 μm and represents the most significant source of uncertainty in quantifying H<sub>2</sub>O content. Thus, we report error bars for H<sub>2</sub>O using the standard deviation of thickness measurements. For each FTIR analysis site we used an aperture of 40 × 40 μm and primarily targeted centers of grains that are clear and free of obvious fluid inclusions. We also analyzed some hazy sites that contain bands of microfluid inclusions to compare with the clear sites. In two samples (14-11-6 and 14-11-11) we analyzed multiple sites (2–7) on several detrital grains to evaluate water

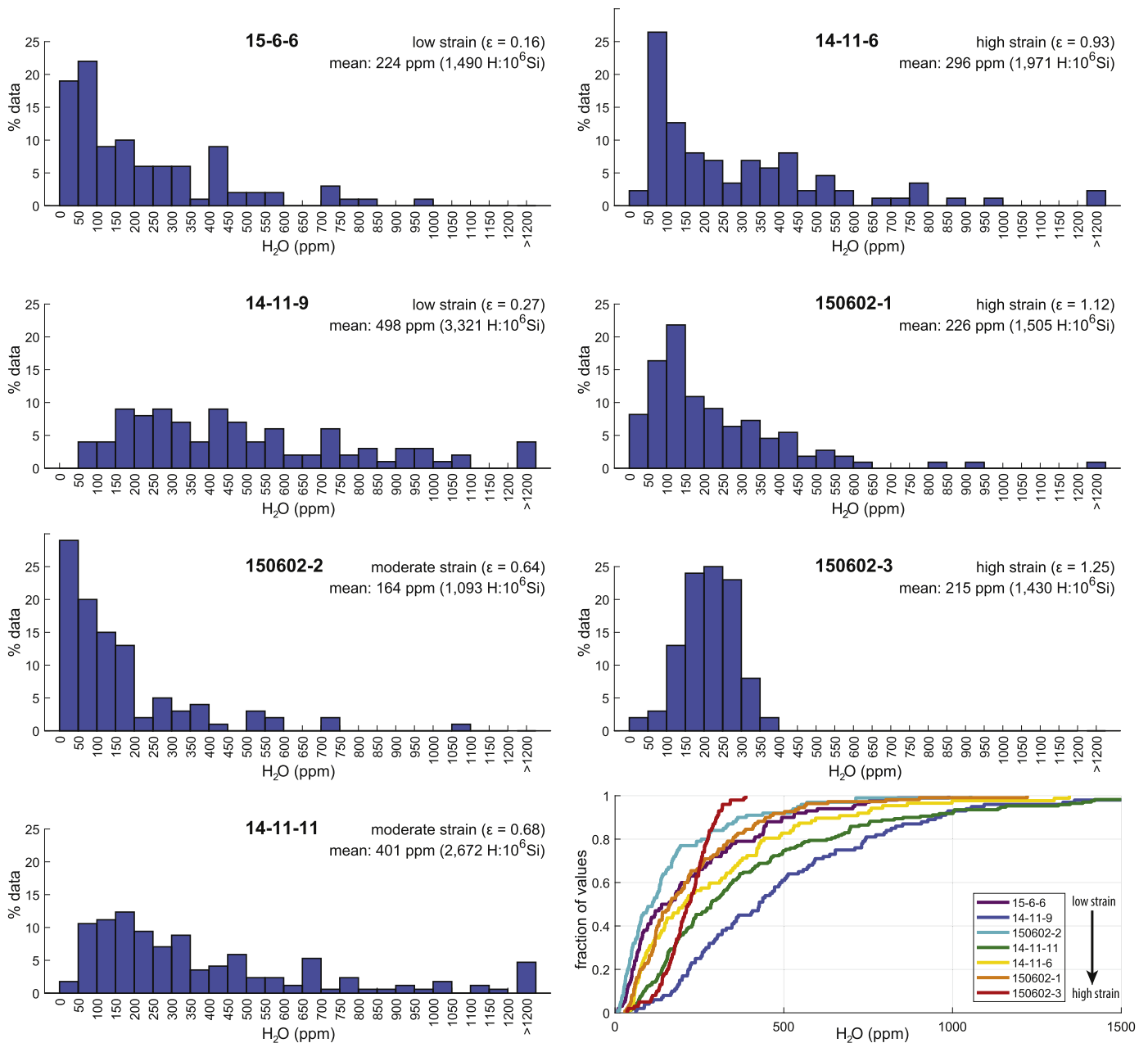


**Fig. 12.** Histograms showing water content in parts per million (ppm) by weight as a percent of the total analyses. Water content was determined by FTIR. The plot on the bottom right shows the cumulative distribution of data from all samples. See **Table 3** for analysis statistics.

content homogeneity at the grain-scale. For each sample we analyzed between 87 and 170 different sites (average 110 sites/sample; Table 3; Supplementary File 5).

#### 4.2.2. FTIR results

FTIR results indicate that water content is heterogeneously distributed throughout the Antietam Formation, ranging from <50 ppm to >1000 ppm by weight in most samples (Fig. 12, Table 3). This heterogeneity is present at the grain scale, as some neighboring grains have water contents that vary by as much as a factor of 10. In addition, individual grains with multiple analyses (in samples 14-11-6 and 14-11-11) reveal local intragranular heterogeneity (Supplementary Files 5, 6). The  $1\sigma$  standard deviation of water content within these grains ranges from <1% to 83% of the mean, with an average standard deviation of 29%. In general, clear spots yielded lower water contents than cloudy spots, but there are several exceptions to this pattern.

Despite the large heterogeneity, it is apparent that on a whole water content in the Antietam Formation is relatively high. The mean water content in all 7 samples ranges from 160 to 500 ppm by weight (1100–3300 H:10<sup>6</sup> Si), and the mean of all 7 samples combined is 290 ppm (1900 H:10<sup>6</sup> Si) (Table 3). These water content values are comparable to “wet” quartz used in dislocation creep experiments, which range from ~1000 to 10,000 H:10<sup>6</sup> Si (e.g., Kronenberg and Wolf, 1990; Paterson and Luan, 1990; Gleason and Tullis, 1995; Stipp et al., 2006). They are also similar to water content values in naturally-deformed quartz inferred to have undergone hydrolytic weakening (Nakashima et al., 1995; Finch et al., 2016; Kronenberg et al., 2020), but are lower than some values documented in natural shear zones (e.g., Kronenberg and Wolf, 1990; Kronenberg et al., 1990). In all samples the Antietam Formation water content is notably higher than values determined for natural samples of “dry” quartz, which are typically ~20–200 H:10<sup>6</sup> Si (e.g., Kronenberg and Wolf, 1990; Gleason and DeSisto, 2008; Menegon et al., 2011; Kilian et al., 2016).

The relationship between water content and strain is unclear, but overall there is a pattern of decreasing water content and variability of water content with increasing strain (Figs. 12, 13). This pattern is most evident in the 4 highest strain samples analyzed via FTIR, and the highest strain sample (150602-3) records the lowest root mean square water content (Fig. 13). This trend is opposite of what might be expected if hydrolytic weakening were largely responsible for strain (e.g., Kronenberg et al., 1990; Nakashima et al., 1995; Gleason and DeSisto, 2008). However, other studies have also noted a clear decrease in water content with strain in naturally-deformed quartzites (Finch et al., 2016;

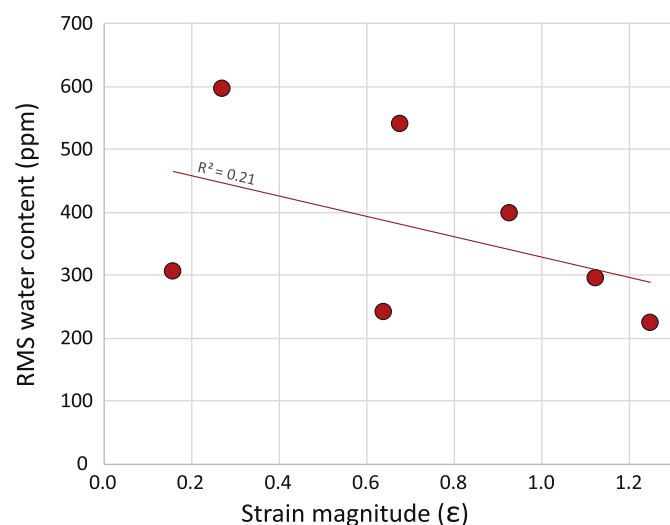


Fig. 13. Plot of root mean square (RMS) water content in ppm by weight vs. octahedral shear strain magnitude ( $\epsilon$ ) for 7 Antietam Formation samples.

Kronenberg et al., 2020) and experimentally-deformed wet quartzite (Post and Tullis, 1998; Stipp et al., 2006; Palazzin et al., 2018). Stipp et al. (2006) and Kronenberg et al. (2020) attribute lower water contents in higher strain samples to migration of water to grain boundaries during deformation, where it may be lost during sample preparation or cannot be accurately analyzed due to grain boundary effects. Water may be transported from grain interiors to boundaries along microcracks or via pipe diffusion along dislocations (e.g., Paterson and Luan, 1990; Bakker and Jansen, 1994; Tarantola et al., 2010). In the Antietam Formation the abundance of fluid-inclusion planes and deformation lamellae lined with fluid inclusions suggest that water was able to migrate to grain boundaries during deformation. Intragranular deformation lamellae and extinction bands are most abundant in the high strain samples, so potential water migration pathways likely increased during strain. High water content along grain boundaries may still promote weakening by enhancing dissolution-precipitation creep and grain-boundary migration/sliding and by increasing water fugacity, which affects dislocation creep flow stress and strain rates. den Brok et al. (1994) documented a significant decrease in the strength of experimentally-deformed quartzite with the addition of water that remained along grain boundaries and microcracks, suggesting infiltration of water into grain interiors is not required for weakening, and that migration of water from grain interiors to boundaries may not result in strengthening.

#### 4.3. Temperature of deformation

##### 4.3.1. Zircon (U–Th)/He thermochronology and thermal modeling

We employed zircon (U–Th)/He thermochronology (ZHe) to assess the thermal history of the Antietam Formation with the goal of constraining the timing and temperature of penetrative deformation. Five zircons from high strain sample 14-11-6 (Table 1, Fig. 6) were randomly selected for (U–Th)/He analysis at the Thermochronology Research and Instrumentation Laboratory at the University of Colorado Boulder (see Stanley and Flowers, 2016 for a description of laboratory techniques). The ZHe dates are 306 Ma, 312 Ma, 331 Ma, 331 Ma, and 453 Ma with a  $2\sigma$  error of  $\pm 7\%$  (Table 4). The anomalously old ~453 Ma grain is much smaller and rounder than the other grains and has a higher effective uranium concentration ( $eU = 252$ ) and lower alpha ejection correction ( $Ft = 0.73$ , Table 4). Accordingly, we consider this grain an outlier and focus our thermal modelling on the 4 zircon grains that range from 306 to 331 Ma, which have a mean date of 320 Ma with a standard deviation of 13 Ma.

Low-temperature thermochronometric dates reflect the integrated thermal history experienced by each grain. When a mineral cools at a constant rate from a high temperature, the observed date can be reliably interpreted to reflect cooling through an effective closure temperature isotherm (~180 °C for zircon, depending upon cooling rate; Dodson, 1979; Reiners et al., 2004; Reiners and Brandon, 2006; Wolfe and Stockli, 2010). In more complex scenarios, such as when cooling histories are non-steady or involve reheating that results in the partial loss of daughter product, the geologic significance of thermochronometric data is less clear. In these cases, numerical models can provide insight into thermal histories consistent with the observed data.

Table 4

Zircon (U–Th)/He data from Antietam Formation sample 14-11-6.  $eU$  = effective uranium ( $U + {}^{235}\text{Th}$ ).  $Ft$  = alpha ejection correction calculated using the method of Ketchum et al. (2011). Corrected date is the alpha-ejection corrected date in Ma. Uncertainty is the full  $2\sigma$  uncertainty.

Sample	$eU$	$Ft$	Corrected Date (Ma)	Uncertainty (Ma)
14-11-6_z01	65.6	0.884	330.9	23.4
14-11-6_z02	199.0	0.886	330.8	23.6
14-11-6_z03	252.5	0.729	452.5	31.6
14-11-6_z04	107.0	0.879	306.1	21.7
14-11-6_z05	78.5	0.882	312.1	22.2

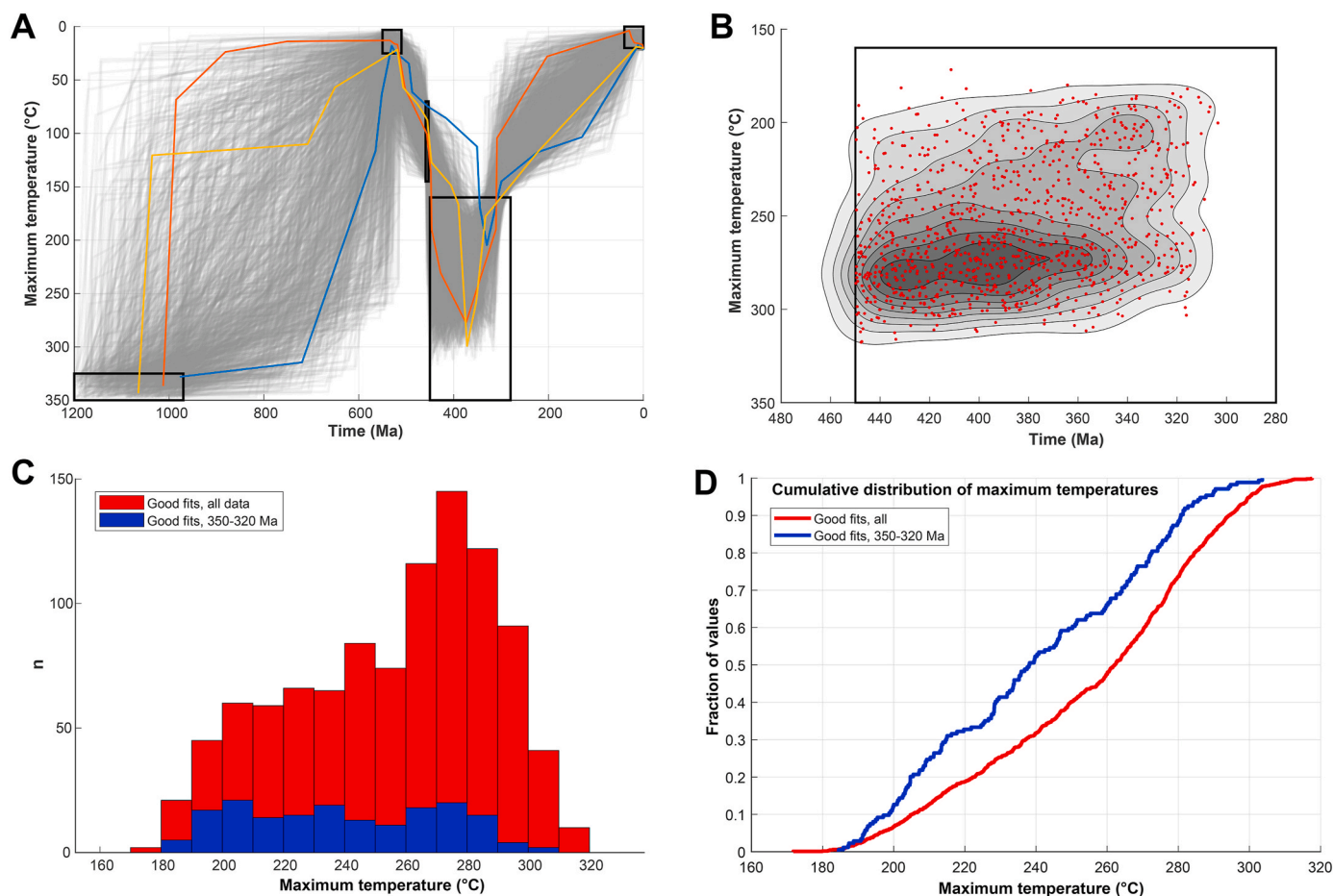


**Fig. 14.** Results from inverse thermal modelling of zircon thermochronology data in HeFTy (Ketcham, 2005), using (U–Th)/He data in Table 4 and a zircon fission track date from sample SNP-32 in Naeser et al. (2016). A) Model time-temperature constraints (black boxes) and 1,000 good paths (gray). The 3 bold colored paths are the 3 best fits to the data as defined by the HeFTy model. See text for details on model constraints. B) Maximum Paleozoic temperature vs. time of maximum temperature from the 1,000 good paths shown in A). Contours of data density were created using a two-dimensional kernel density algorithm (Botev et al., 2010). C) Histogram of maximum Paleozoic temperature for all 1,000 good paths (red) and good paths that have maximum temperatures within ~350–320 Ma (blue), the most likely timeframe of penetrative deformation in the western Blue Ridge. D) Cumulative distribution of maximum temperature values from data in C). (For interpretation of the references to color in this figure legend, the reader is referred to the Web version of this article.)

To explore thermal histories consistent with available thermochronometric and geologic data, we utilized the modeling program HeFTy (Ketcham, 2005). For a given time-temperature history, HeFTy can predict fission-track and (U–Th)/He dates that can be compared to observed dates to assess the quality of the fit. Using an inverse modelling approach, HeFTy can randomly generate many model time-temperature history paths and identify those that provide the best match to the observed data. Although model results are non-unique, as many possible time-temperature paths may produce a similar date, modeling can place bounds on the possible range of time-temperature histories.

We incorporated known geologic constraints into inverse modeling of the Antietam zircon data (Fig. 14A). Zircon U–Pb data from the Chilhowee Group are comprised almost entirely of grains between 1250 and 1000 Ma, indicating a Grenvillian affinity (Thomas et al., 2017). In HeFTy, the thermal history for each zircon grain initiates at a temperature >320 °C before 980 Ma, above the fission track partial annealing zone. All grains must have been exhumed by the latest Proterozoic to earliest Cambrian, prior to deposition of the Antietam Formation. Biostratigraphic constraints place deposition of the Chilhowee Group between 563 and 516 Ma (Smoot and Southworth, 2014). In HeFTy, our thermal histories are required to pass through a temperature <25 °C sometime during this time interval. Post-depositional burial must have heated the Antietam Formation. The Chilhowee Group is

stratigraphically below a thick section of Paleozoic marine strata, including several kilometers of Cambrian to Ordovician strata that were deposited along a passive margin during a tectonically quiescent period. This passive margin shelf was drowned during the Ordovician Taconic Orogeny, the onset of which is recorded by flysch deposits of the Martinsburg Formation (Bradley, 1989). In the Front Royal area the base of the Antietam Formation was buried beneath ~2.8–4.1 km of stratigraphic section prior to deposition of the Martinsburg Formation (Wickham, 1972; Rader and Biggs, 1975; Lukert and Nuchols, 1976; Fichter et al., 2010). Based on pre-Taconic burial, we constrain the Antietam Formation zircons to pass between 70 °C and 145 °C at the onset of Martinsburg Formation deposition (middle to upper Sandbian, ~455 Ma; Ross et al., 1982). After this time, the zircons must have been heated >160 °C to partially or fully reset the zircon (U–Th)/He system. The final constraint applied to our thermal model is that the rocks are required to reach near-surface conditions ( $T < 25$  °C) sometime in the past 50 Myr.

In addition to data from 4 zircon (U–Th)/He analyses, our inverse HeFTy model also incorporates a published  $611 \pm 105$  Ma zircon fission-track date from a Harpers Formation sample collected ~430 m SSE of our zircon (U–Th)/He sample (Naeser et al., 2016). Independent of the thermal model, this date indicates that strata directly below the Antietam Formation were never heated enough to fully anneal Proterozoic

zircon fission tracks. We generated 1000 “good” time-temperature paths in HeFTy and calculated the maximum Paleozoic temperature achieved by each path (Fig. 14A and B). The vast majority of peak temperatures from these paths are between 180 °C and 310 °C, with a mode of 270–280 °C (Fig. 14C). The timing of peak heating varies between ~310 Ma to 450 Ma without a clear mode (Fig. 14B). In general, paths that have earlier peak heating are associated with higher maximum temperatures (Fig. 14B). The three best fits to the data out of the 1000 good paths yield a peak temperature ranging from ~210 to 300 °C at ~370–330 Ma (Fig. 14A). White mica (muscovite/sericite)  $^{40}\text{Ar}/^{39}\text{Ar}$  dates from the Virginia Blue Ridge largely cluster between ~350 Ma to 320 Ma (Bailey et al., 2007b; Jenkins et al., 2012; Bailey, 2016). In the western Blue Ridge, these dates are interpreted to record the timing of mica growth and penetrative deformation (Bailey et al., 2006, 2007b; Jenkins et al., 2012; Bailey, 2016). Accordingly, it is likely that the penetrative strain in the Antietam Formation also occurred in this Mississippian window, in between the time interval typically assigned to the Acadian and Alleghanian orogenies. Model peak temperatures that fall within this preferred ~350–320 Ma window primarily range from 190 °C to 290 °C, with a mean peak temperature of 240 °C  $\pm$  a standard deviation of 32 °C (Fig. 14C). Approximately 97% of these paths yield peak temperatures  $\leq$ 290 °C (Fig. 14D). The thermal model does not favor a specific temperature below 290 °C, but we interpret the model to provide strong evidence that penetrative deformation in the Antietam Formation occurred below 290 °C.

#### 4.3.2. Quartz *c*-axis opening angle thermometry

The opening-angle of quartz *c*-axes in the X:Z reference frame has been calibrated for deformation temperatures between ~250 °C and 1050 °C (Kruhl, 1998; Morgan and Law, 2004; Law, 2014; Faleiros et al., 2016). A linear relationship between opening angle and temperature most likely reflects the temperature dependence of prism [*c*] vs. basal <*a*> slip in quartz, with higher temperatures facilitating prism [*c*] slip and reorientation of *c*-axes towards the fabric attractor. Temperatures derived from opening angles are typically assigned a  $\pm$ 50 °C error based on uncertainties in the calibration and petrological thermometry, although the true precision for this thermometer is not well known.

Five of the 6 Antietam Formation samples analyzed by EBSD yielded moderately to well-defined *c*-axis opening angles (Fig. 10). We estimated opening angles manually from these pole figures and by using the automated symmetry analysis method of Hunter et al. (2018) in MTEX (Table 3). Opening angles using the Hunter et al. (2018) method were determined using two contour smoothing options (5° and 10° half-widths), resulting in 3 opening-angle estimates per sample (Table 2). In 4 of the 5 samples the average opening angle yields temperatures between 245  $\pm$  50 °C to 298  $\pm$  50 °C based on the calibration of Faleiros et al. (2016). One sample yielded an anomalously high temperature of 386  $\pm$  50 °C, which is unrealistically high given results from thermal modeling. This particular sample is notably lower strain than the other samples analyzed via EBSD and has a larger component of flattening strain (Table 2). Given the relatively low strain and CPO strength, we consider this temperature estimate unreliable. The remaining 4 samples have a mean temperature of 264 °C, and the most well-defined *c*-axis opening angles (samples 14-11-6 and 14-11-11) yield temperatures of 255  $\pm$  50 °C and 245  $\pm$  50 °C. The highest strain sample (150602-1) did not yield an opening angle, as *c*-axes form one broad point maxima about the Z-axis (Fig. 10, Table 2). It is worth noting that the *c*-axis opening angle thermometer has rarely been applied to samples naturally deformed at <300 °C. Deformation experiments by Tullis et al. (1973) suggest that dislocation creep under low temperature/high strain rate conditions results in development of *c*-axis maxima patterns, whereas higher temperature/lower strain rate conditions result in small-circle girdle distributions of *c*-axes and opening angles. In the Antietam Formation samples, the mix of broad *c*-axis maxima and two point maxima weakly connected by small circle girdles may represent CPOs characteristic of natural quartz dislocation creep at <300 °C.

Water content, strain rate, and strain geometry also most likely influence *c*-axis opening angles. At a given temperature, higher degrees of hydrolytic weakening, slower strain rates, and a greater component of flattening strain should all contribute to larger opening angles (Law, 2014). Law (2014) suggests that the  $\pm$ 50 °C error on the opening-angle thermometer most likely encompasses uncertainty due to variable strain rates and water contents in typical L-S tectonites. In S- and S>L tectonites, however, opening angles may be increased by several degrees due to flattening strain (e.g.,  $\sim$ 5° greater for pure flattening vs. plane strain according to one numerical model from Lister and Hobbs, 1980; Law, 2014). According to the Faleiros et al. (2016) calibration, a 1° difference in opening angle corresponds to 4.6 °C difference in temperature. The quantitative relationship between strain geometry and opening angle is not currently clear, but it is possible that opening angle temperatures derived from the Antietam Formation *c*-axis patterns slightly overestimate temperature.

#### 4.4. Strain rate and strength profile

The strain rate during dislocation creep can be quantified with flow laws, which relate strain rate to differential stress, temperature, water fugacity, material parameters, and activation energy. Several studies have developed constitutive strain rate equations for quartzite dislocation creep (e.g., Luan and Paterson, 1992; Gleason and Tullis, 1995; Hirth et al., 2001; Rutter and Brodie, 2004; Tokle et al., 2019). However, published quartzite flow laws may yield significantly different strain rates for a given set of conditions, and the selection of which flow law to apply is not straightforward. The high stress flow law parameters developed by Tokle et al. (2019) appear to be particularly well suited for estimating dislocation creep strain rates in the Antietam Formation given deformation mechanisms and conditions we have documented. This flow law provides a good fit to laboratory data of wet quartzite that has undergone basal <*a*> slip at relatively low temperature and high stress conditions (Tokle et al., 2019), consistent with Antietam Formation deformation.

We modelled the strength profile of the Antietam Formation assuming typical frictional slip criteria for a thrust regime after Byerlee (1978), a vertical stress governed by an average overburden rock density of 2600 kg/m<sup>3</sup>, a geothermal gradient of 25 °C/km and a surface temperature of 15 °C, dislocation creep based on the Tokle et al. (2019) extrapolated fit quartzite flow law, and a water fugacity that varies with temperature and a fluid pressure equal to the vertical stress (Fig. 15). For strain rate calculations we estimate deformation temperatures in the Antietam Formation to be ~250–280 °C, which encompasses the majority of temperatures calculated from *c*-axis opening angle thermometry and thermal modelling. We estimate stresses from dynamically recrystallized grain size using the Stipp and Tullis (2003) piezometer (~200  $\pm$  59 MPa, Fig. 9), consistent with the Tokle et al. (2019) flow law analysis. These constraints indicate a strain rate of  $\sim$ 10<sup>-15</sup>/s<sup>-1</sup>, ranging from  $\sim$ 2  $\times$  10<sup>-16</sup>/s<sup>-1</sup> to  $\sim$ 8  $\times$  10<sup>-15</sup>/s<sup>-1</sup> (Fig. 15). For the same conditions the Hirth et al. (2001) quartzite flow law yields strain rates that are nearly an order of magnitude faster (Fig. 15). Application of the Holyoke and Kronenberg (2010) piezometer correction lowers the Tokle et al. (2019) flow law strain rates by ~61%, with an average of  $\sim$ 4  $\times$  10<sup>-16</sup>/s<sup>-1</sup>. Given these constraints on strain rate and our strain analysis results, we can calculate the strain time interval assuming steady state dislocation creep. The 5 highest strain Antietam Formation samples record an average axial shortening of ~50% ( $\epsilon = -0.50$ ), and dynamically recrystallized grain sizes in these samples correlate to an average differential stress of ~215 MPa according to the Stipp and Tullis (2003) piezometer (Table 1, Fig. 9). At ~10 km depth (~265 °C) the Tokle et al. (2019) flow law used in our model corresponds with a strain rate of  $\sim$ 1.7  $\times$  10<sup>-15</sup>/s<sup>-1</sup>, which would accumulate 50% shortening in ~9 Myr. This time interval is reasonable given the evidence for protracted Mississippian tectonism in the Blue Ridge (e.g., Bailey et al., 2006).

In our stress profile model, the rock strength predicted by the Byerlee

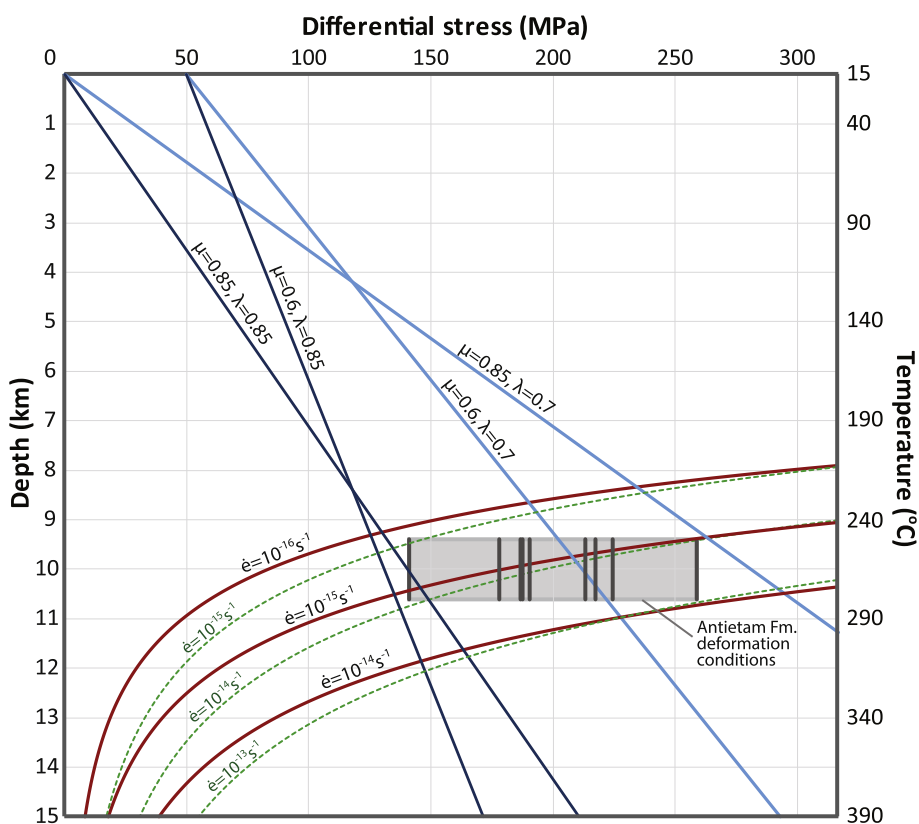


**Fig. 15.** Stress profile model of the Antietam Formation. Blue lines are frictional sliding criteria for a thrust regime based on Byerlee (1978) ( $\sigma_s = 0.85 \sigma_n$  and  $\sigma_s = 50 \text{ MPa} + 0.6 \sigma_n$ ) and fluid pressure that is 70% ( $\lambda = 0.7$ ) to 85% ( $\lambda = 0.85$ ) of the vertical stress, assuming an average overburden density of 2.6  $\text{g}/\text{cm}^3$ . The red curves are wet quartzite flow laws based on the extrapolated fit of Tokle et al. (2019), assuming a surface temperature of 15 °C, a geothermal gradient of 25 °C/km, and a water fugacity that varies with temperature and a fluid pressure equal to the vertical stress (calculated using T. Withers' fugacity calculator, [www.esci.umn.edu/people/researchers/withe012/fugacity.htm](http://www.esci.umn.edu/people/researchers/withe012/fugacity.htm)). The dashed green curves are quartzite flow laws derived by Hirth et al. (2001).  $\dot{\epsilon}$  = strain rate in seconds. The gray box outlines the temperature (~250–280 °C) and differential stress conditions we estimate for the Antietam Formation, with stress derived from the Stipp and Tullis (2003) quartz dynamically recrystallized piezometer of 9 samples (shown as the vertical gray bars). (For interpretation of the references to color in this figure legend, the reader is referred to the Web version of this article.)

(1978) frictional sliding criteria near the brittle-plastic transition is consistent with stresses inferred from grain size piezometry if fluid pressure is ~70–85% of the vertical stress ( $\lambda = 0.7$ –0.85; Fig. 15). High fluid pressure is also consistent with evidence for localized brittle deformation in the 3 highest strain samples. Dynamically recrystallized grain size in these 3 samples records a mean differential stress of ~232 MPa (using the Stipp and Tullis (2003) piezometer), most likely at a depth of ~10 km (vertical  $\sigma \approx 255 \text{ MPa} = \sigma_3$  assuming an Andersonian stress regime for thrust faulting; Anderson, 1951). Based on these conditions, to achieve brittle failure according to Byerlee's Law where  $\sigma_s = 0.85 \sigma_n$  for  $\sigma_n < 200 \text{ MPa}$  and  $\sigma_s = 50 \text{ MPa} + 0.6 \sigma_n$  for  $\sigma_n > 200 \text{ MPa}$  (also an approximation of typical Coulomb failure), a fluid pressure equal to 75–90% of the vertical stress is required (Fig. 16).

## 5. Discussion

### 5.1. Structural context of coaxial strain in the Antietam Formation

The high-strain zone we have documented in the Antietam Formation developed primarily as a discrete zone of coaxial flattening, perhaps locally associated with a component of top-NW shear (e.g., based on crystallographic fabrics in sample 15-6-8, Fig. 10). Penetrative fabrics in this zone are oriented at a high angle to bedding but record evidence for folding about a gently NE-plunging axis (Figs. 2, 3), indicating that development of this high strain zone postdated some but not all folding of Cambrian units in this part of the Blue Ridge. The high angle between bedding and these fabrics indicates that the high strain zone cuts across stratigraphy, and that strain was not localized parallel to mechanical stratigraphy (Fig. 2). Zircon (U–Th)/He data and thermal modeling suggest that this penetrative strain developed coevally with Mississippian NW-directed shortening in the Blue Ridge basement but prior to Alleghanian shortening of the Appalachian foreland fold-and-thrust belt (Table 4, Fig. 14). As shortening migrated westward into the Valley and Ridge, the high strain zone was most likely folded and rapidly exhumed

in the hanging wall of a structurally lower thrust fault in the Late Mississippian and/or Early Pennsylvanian.

Based on these observations and data, we propose that coaxial flattening in the Antietam Formation developed as a weak zone in the hanging wall of the Happy Creek thrust fault and in the footwall of a NW-vergent thrust system. This zone cut across stratigraphy but potentially paralleled the Happy Creek thrust fault below and the basement-involved thrust system above. Coaxial flattening may have initiated in response to tectonic burial by the NW-vergent thrust system, along which noncoaxial shear was focused. To localize coaxial strain in this zone, however, a weakness discordant to stratigraphy must have developed. The high strain zone appears to be localized near the top or structurally just above a breccia zone in the Antietam Formation (Fig. 2). These breccia zones may have multiple origins (Stose et al., 1919; Southworth et al., 2009; Carmichael et al., 2017), but the map distribution of breccia along the trace of the Happy Creek thrust fault suggests at least a component of this breccia zone is associated with thrust deformation along the fault (Wickham, 1972; Rader and Biggs, 1975). The high fracture porosity in this breccia zone may have facilitated fluid infiltration into the Antietam Formation near the top of the zone, creating a hydrolytically weakened zone that localized penetrative strain. If correct, this structural model indicates that discrete coaxial shear zones may develop due to fluid infiltration and hydrolytic weakening facilitated by brittle deformation.

### 5.2. Low-temperature dislocation creep in quartzite

We have presented evidence that dislocation creep is the dominant deformation mechanism in the Antietam Formation high-strain zone, with basal  $\langle a \rangle$  glide accommodating the majority of penetrative strain. Widespread development of deformation lamellae and minor subgrain development, grain boundary bulging, and dynamic recrystallization also record crystal plasticity. This crystal plastic strain occurred in “wet” conditions with high intragranular water content, differential stresses

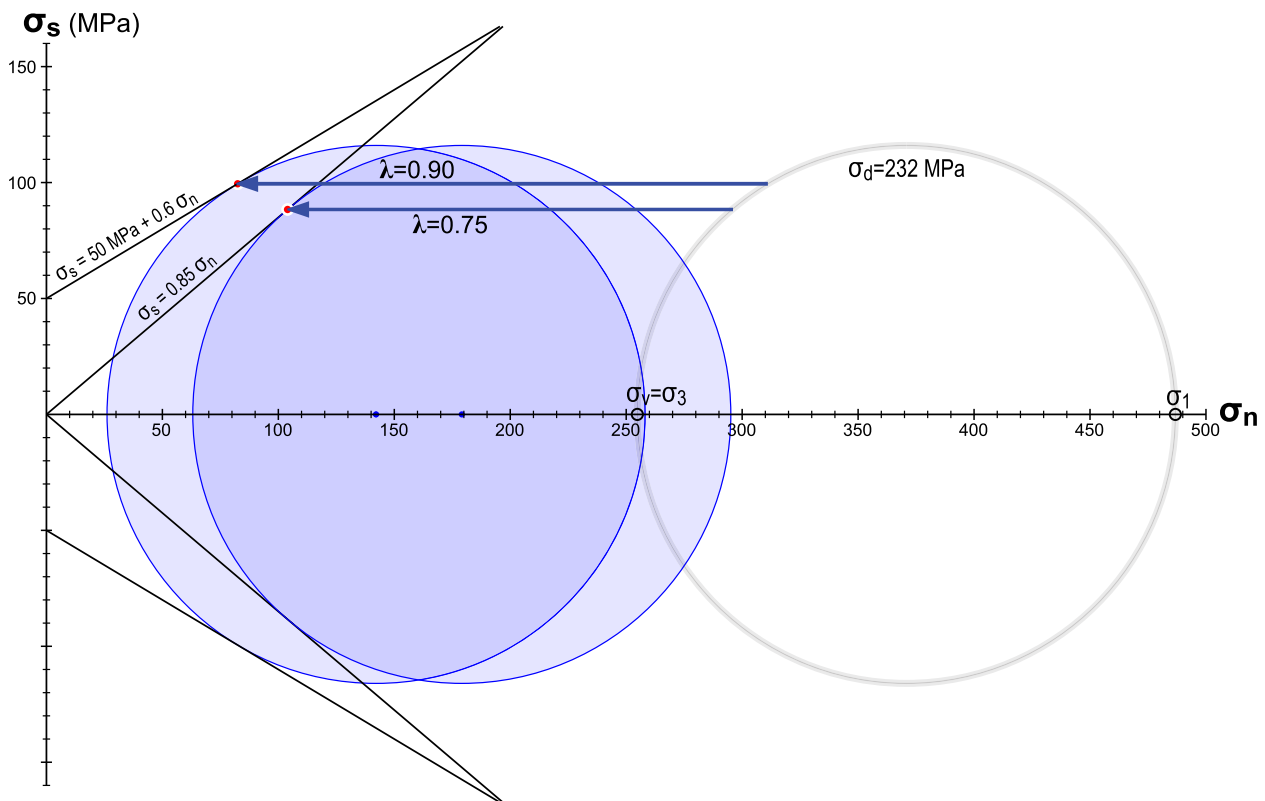


**Fig. 16.** Mohr diagram modelling stress and fluid pressure required for brittle failure of the Antietam Formation near the brittle-plastic transition. The differential stress ( $\sigma_d$ , diameter of the Mohr circle) is based on the [Stipp and Tullis \(2003\)](#) piezometer for a mean dynamically recrystallized grain size of  $\sim 3.8 \mu\text{m}$  in the 3 highest strain Antietam Formation samples, which record evidence of brittle-plastic deformation. The frictional sliding envelopes are based on Byerlee's Law for normal stress  $< 200 \text{ MPa}$  ( $\sigma_s = 0.85 \sigma_n$ ) and  $> 200 \text{ MPa}$  ( $\sigma_s = 50 \text{ MPa} + 0.6 \sigma_n$ ), where  $\sigma_s$  = shear stress and  $\sigma_n$  = normal stress ([Byerlee, 1978](#)).  $\lambda$  = the pore fluid pressure ratio required for brittle failure of an optimally oriented fracture (= pore fluid pressure/vertical stress), illustrated by the critical effective stress (blue Mohr circles). (For interpretation of the references to color in this figure legend, the reader is referred to the Web version of this article.)

that were likely  $\sim 200 \pm 59 \text{ MPa}$ , and temperatures below the oft-cited  $\sim 300 \text{ }^\circ\text{C}$  for the quartz brittle-plastic transition. The most well-defined *c*-axis opening angles suggest a deformation temperature of  $\sim 250 \text{ }^\circ\text{C}$ , and the mean temperature from all clear *c*-axis opening angles is  $\sim 264 \text{ }^\circ\text{C}$ . Our thermal modeling indicates that maximum temperatures in the likely deformation timeframe (350–320 Ma) were  $< 290 \text{ }^\circ\text{C}$ , and the average maximum temperature generated by good-fit time-temperature paths in this timeframe is  $\sim 240 \text{ }^\circ\text{C} \pm 32 \text{ }^\circ\text{C}$ . Taken together, we suggest that the deformation temperature was  $\sim 240\text{--}290 \text{ }^\circ\text{C}$  and most likely  $\sim 250\text{--}280 \text{ }^\circ\text{C}$ . These temperatures are low for quartzite that has undergone a significant amount of dislocation creep, but they are not anomalous for strained quartz-rich rocks in a thrust regime, where the brittle strength of the crust is typically high. Several studies have suggested quartz dislocation creep in a thrust regime may occur at these temperatures ([Voll, 1976](#); [Dunlap et al., 1997](#); [van Daalen et al., 1999](#); [Trepman and Stöckhert, 2009](#); [Kidder et al., 2012](#)), and we note that the temperature and differential stresses we estimate for the Antietam Formation match those estimated for the quartz brittle-plastic transition in a study by [Kidder et al. \(2012\)](#). Based on our constraints on deformation conditions and an appropriate wet quartzite flow law ([Tokle et al., 2019](#)), we estimate plastic strain rates to be  $\sim 10^{-15}/\text{s}^{-1}$  with a range from  $\sim 2 \times 10^{-16}/\text{s}^{-1}$  to  $\sim 8 \times 10^{-15}/\text{s}^{-1}$  ([Fig. 15](#)). These strain rates are relatively slow but still within the normal range for most shear zones, which typically record strain rates between  $10^{-11}/\text{s}^{-1}$  and  $10^{-15}/\text{s}^{-1}$  (e.g., [Pfiffner and Ramsay, 1982](#); [Carter and Tsenn, 1987](#); [Behr and Platt, 2014](#)). The peak strength recorded by dynamic recrystallization near the brittle-plastic transition matches the strength predicted by typical ([Byerlee, 1978](#)) friction where fluid pressure is high

( $\sim 70\text{--}85\%$  of the vertical stress; [Fig. 15](#)). This high fluid pressure is independently supported by evidence for brittle failure in the highest strain samples, requiring a fluid pressure of  $75\text{--}90\%$  of the vertical stress for [Byerlee \(1978\)](#) frictional sliding and typical Coulomb failure criteria ([Fig. 16](#)). High fluid pressure characterizes many thrust regimes (e.g., [Hubbert et al., 1959](#); [Davis et al., 1983](#)), so none of the deformation conditions we estimate for the Antietam Formation high strain zone appear to be anomalous. The quantitative effects of intragranular water content on dislocation creep are difficult to evaluate, particularly if fluids migrate to grain boundaries during deformation, as we infer for the Antietam Formation (section 4.2.2.). However, it is clear that intragranular water content in the Antietam Formation is high ( $1100\text{--}3300 \text{ H:}10^6\text{Si}$ ), although not anomalously high for “wet” quartz (e.g., [Kronenberg and Wolf, 1990](#)), and associated hydrolytic weakening undoubtedly helped facilitate dislocation creep at low temperatures. Thus, low-temperature dislocation creep in the Antietam Formation was enabled by relatively slow strain rates and high intragranular water content, but these conditions are within the normal range of natural quartzites in thrust regimes. The minimum temperature for quartz plasticity is clearly not a fixed boundary and can be as low  $\sim 250\text{--}280 \text{ }^\circ\text{C}$  given certain conditions.

## 6. Conclusions

We present macro- and microstructural data, 3D strain analyses, EBSD data, FTIR analyses, and low-temperature thermochronology data to document the development of high strain fabrics in Antietam Formation quartzite along the western flank of the Blue Ridge in northern

Virginia. These high strain fabrics developed as a zone of coaxial flattening that cut across stratigraphy, potentially localized via hydrolytic weakening from fluid infiltration above the Happy Creek thrust fault breccia zone. Dislocation creep was the dominant deformation mechanism, with basal  $\langle a \rangle$  glide accommodating most strain. Detailed FTIR analyses indicate high intragranular water content (1100–3300 H:10<sup>6</sup>Si, or ~160–500 ppm by weight). This high water content likely enhanced dislocation creep via hydrolytic weakening, although overall water content appears to decrease with strain, suggesting water migrated to grain boundaries during deformation. Quartz *c*-axis opening-angle thermometry suggest deformation temperatures of  $245 \pm 50$  °C to  $298 \pm 50$  °C (mean value = 264 °C). Thermal modeling of zircon thermochronology data indicate that peak temperatures were <290 °C during Mississippian deformation. Altogether these data suggest dislocation creep occurred at ~250–280 °C, which is below what is typically considered the brittle-plastic transition in quartz. Based on this temperature range and differential stresses from dynamically recrystallized grain size piezometry (~200 ± 59 MPa), we estimate a strain rate of ~10<sup>-15</sup> s<sup>-1</sup>. Peak stress near the brittle-plastic transition matches stress governed by Byerlee's Law (Byerlee, 1978) and high fluid pressure estimated to be 70–85% lithostatic stress. High intragranular water content and relatively low strain rates enabled dislocation creep to occur at relatively low temperatures. Water content in natural shear zones is usually unknown, but the water content values we determine for the Antietam Formation high-strain zone are comparable to values in “wet” quartzite used in deformation experiments. None of the deformation conditions we document in the Antietam Formation appear to be anomalous, suggesting unique circumstances are not required for quartz dislocation creep to occur at such low temperatures.

#### CRedit authorship contribution statement

**John S. Singleton:** Conceptualization, Methodology, Validation, Formal analysis, Investigation, Writing - original draft, Writing - review & editing, Visualization, Project administration, Funding acquisition. **Jeffrey M. Rahl:** Conceptualization, Methodology, Software, Formal analysis, Investigation, Resources, Writing - review & editing, Visualization. **Kenneth S. Befus:** Methodology, Formal analysis, Investigation, Resources, Writing - review & editing.

#### Declaration of competing interest

The authors declare that they have no known competing financial interests or personal relationships that could have appeared to influence the work reported in this paper.

#### Acknowledgements

We thank Carlin Green for assistance with some of the strain analyses. Rick Law, Dyanna Czeck, and editor Stephen Laubach provided insightful reviews that have improved this manuscript. This research has benefited from discussions of Virginia geology with Chuck Bailey, Scott Southworth, Dan Doctor, Callan Bentley, and Rick Diecchio. Funding was provided primarily by internal awards at George Mason University and Colorado State University to JS. Research support was also provided by National Science Foundation grant EAR-1724429 to KB.

#### Appendix A. Supplementary data

Supplementary data to this article can be found online at <https://doi.org/10.1016/j.jsg.2020.104109>.

#### References

Anders, M.H., Laubach, S.E., Scholz, C.H., 2014. Microfractures: a review. *J. Struct. Geol.* 69, 377–394. <https://doi.org/10.1016/j.jsg.2014.05.011>.

- Anderson, E.M., 1951. *The Dynamics of Faulting*, second ed. Oliver and Boyd, Edinburgh, U. K, p. 183.
- Bailey, C.M., 2016. The Central and Southern Appalachian Blue Ridge province: along-strike variation at the Appalachian Orogen's thick- to thin-skinned deformation front. *Geol. Soc. Am. Abstr. Progr.* 48 (7).
- Bailey, C.M., Simpson, C., De Paor, D.G., 1994. Volume loss and tectonic flattening strain in granitic mylonites from the Blue Ridge province, central Appalachians. *J. Struct. Geol.* 16 (10), 1403–1416.
- Bailey, C.M., Southworth, S., Tollo, R.P., Pazzaglia, F.J., 2006. Tectonic History of the Blue Ridge, North-Central Virginia. *Excursions in Geology and History: Field Trips in the Middle Atlantic States*, vol. 8. Geological Society of America Field Guide, pp. 113–134.
- Bailey, C.M., Polvi, L.E., Forte, A.M., 2007a. Pure shear dominated high-strain zones in basement terranes. In: Hatcher Jr., R.D., Carlson, M.P., McBride, J.H., Martínez Catalán, J.R. (Eds.), *4-D Framework of Continental Crust*. Geological Society of America Memoir, pp. 93–108, 200.
- Bailey, C.M., Kunk, M.J., Southworth, C.S., Wootton, K.M., 2007b. Late paleozoic orogenesis in the Virginia Blue Ridge and piedmont: a view from the south. *Geol. Soc. Am. Abstr. Progr.* 39 (1).
- Bakker, R.J., Jansen, J.B.H., 1994. A mechanism for preferential H<sub>2</sub>O leakage from fluid inclusions in quartz, based on TEM observations. *Contrib. Mineral. Petrol.* 116, 7–20.
- Behr, W.M., Platt, J.P., 2011. A naturally constrained stress profile through the middle crust in an extensional terrane. *Earth Planet. Sci. Lett.* 303 (3–4), 181–192.
- Behr, W.M., Platt, J.P., 2013. Rheological evolution of a Mediterranean subduction complex. *J. Struct. Geol.* 54, 136–155.
- Behr, W.M., Platt, J.P., 2014. Brittle faults are weak, yet the ductile middle crust is strong: implications for lithospheric mechanics. *Geophys. Res. Lett.* 41 (22), 8067–8075.
- Blacic, J.D., 1975. Plastic-deformation mechanisms in quartz: the effect of water. *Tectonophysics* 27 (3), 271–294.
- Blenkinsop, T.G., Drury, M.R., 1988. Stress estimates and fault history from quartz microstructures. *J. Struct. Geol.* 10 (7), 673–684.
- Botev, Z.I., Grotowski, J.F., Kroese, D.P., 2010. Kernel density estimation via diffusion. *Ann. Stat.* 38 <https://doi.org/10.1214/10-AOS799>.
- Bradley, D.C., 1989. Taconic plate kinematics as revealed by foredeep stratigraphy, Appalachian orogen. *Tectonics* 8 (5), 1037–1049.
- Bunge, H., 1982. *Texture Analysis in Materials Science: Mathematical Models*. Butterworths, London, p. 593.
- Byerlee, J., 1978. Friction of rocks: pure appl. Geophysics 116, 615–626.
- Carmichael, S.K., Doctor, D.H., Wilson, C.G., Feierstein, J., McAleer, R.J., 2017. New insight into the origin of manganese oxide ore deposits in the Appalachian Valley and Ridge of northeastern Tennessee and northern Virginia, USA. *GSA Bulletin* 129 (9–10), 1158–1180.
- Carter, N.L., Tsenn, M.C., 1987. Flow properties of continental lithosphere. *Tectonophysics* 136, 27–63.
- Davis, D., Suppe, J., Dahlen, F.A., 1983. Mechanics of fold-and-thrust belts and accretionary wedges. *J. Geophys. Res.* 88, 1153–1172.
- den Brok, B., Meinecke, J., Röller, K., 1994. Fourier transform IR-determination of intragranular water content in quartzites experimentally deformed with and without added water in the ductile deformation field. *J. Geophys. Res.: Solid Earth* 99 (B10), 19821–19828.
- Derez, T., Pennock, G., Drury, M., Sintubin, M., 2015. Low-temperature intracrystalline deformation microstructures in quartz. *J. Struct. Geol.* 71, 3–23.
- Dodson, M.H., 1979. Theory of cooling ages. In: Jager, E., Hunziker, J.C. (Eds.), *Lectures in Isotope Geology*. Springer, Berlin, pp. 194–202.
- Drury, M.R., 1993. Deformation lamellae in materials and minerals. In: Noland, J.N., Fitz Gerald, J.D. (Eds.), *Defects and Processes in the Solid State: Geosciences Applications, the McLaren Volume*. Elsevier Science Publishers.
- Dunlap, W.J., Hirth, G., Teyssier, C., 1997. Thermomechanical evolution of a ductile duplex. *Tectonics* 16 (6), 983–1000.
- Edmondson, R.S., Nunan, W.E., 1973. *Geology of the Berryville, Stephenson, and Boyce Quadrangles, Virginia: Virginia Division of Mineral Resources, Report of Investigations, vol. 34 scale 1:24,000*.
- Faleiros, F.M., da Cruz Campanha, G.A., da Silveira Bello, R.M., Fuzikawa, K., 2010. Quartz recrystallization regimes, *c*-axis texture transitions and fluid inclusion reequilibration in a prograde greenschist to amphibolite facies mylonite zone (Ribeira Shear Zone, SE Brazil). *Tectonophysics* 485 (1–4), 193–214.
- Faleiros, F.M., Moraes, R.D., Pavan, M., Campanha, G.A.D.C., 2016. A new empirical calibration of the quartz *c*-axis fabric opening-angle deformation thermometer. *Tectonophysics* 671, 173–182.
- Fellows, R.E., 1943. Recrystallization and flowage in Appalachian quartzite. *Bull. Geol. Soc. Am.* 54 (9), 1399–1432.
- Fichter, L.S., Whitmeyer, S.J., Bailey, C.M., Burton, W., 2010. Stratigraphy, structure, and tectonics: an east-to-west transect of the Blue Ridge and Valley and Ridge provinces of northern Virginia and West Virginia. *Field Guides* 16, 103–125.
- Finch, M.A., Weinberg, R.F., Hunter, H.J.R., 2016. Water loss and the origin of thick ultramylonites. *Geology* 44, 599–602.
- Fossen, H., 2016. *Structural Geology*, second ed. Cambridge University Press, Cambridge, p. 510.
- Gleason, G.C., DeSisto, S., 2008. A natural example of crystal-plastic deformation enhancing the incorporation of water into quartz. *Tectonophysics* 446 (1–4), 16–30.
- Gleason, G.C., Tullis, J., 1995. A flow law for dislocation creep of quartz aggregates determined with the molten salt cell. *Tectonophysics* 247 (1–4), 1–23.
- Gottardi, R., Teyssier, C., 2013. Thermomechanics of an extensional shear zone, Raft River metamorphic core complex, NW Utah. *J. Struct. Geol.* 53, 54–69.

- Griggs, D., 1967. Hydrolytic weakening of quartz and other silicates. *Geophys. J. Int.* 14 (1–4), 19–31.
- Gueydan, F., Mehl, C., Parra, T., 2005. Stress-strain rate history of a midcrustal shear zone and the onset of brittle deformation inferred from quartz recrystallized grain size. *Geol. Soc. Lond. Special Publ.* 243 (1), 127–142.
- Hatcher Jr., R.D., 1989. Tectonic Synthesis of the US Appalachians. The Appalachian-Ouachita Orogen in the United States: Boulder, Colorado, vol. 2. Geological Society of America, *Geology of North America*, pp. 511–535.
- Hielscher, R., Schaeben, H., 2008. A novel pole figure inversion method: specification of the MTEX algorithm. *J. Appl. Crystallogr.* 41 (6), 1024–1037.
- Hirth, G., Tullis, J.A.N., 1992. Dislocation creep regimes in quartz aggregates. *J. Struct. Geol.* 14 (2), 145–159.
- Hirth, G., Teyssier, C., Dunlap, J.W., 2001. An evaluation of quartzite flow laws based on comparisons between experimentally and naturally deformed rocks. *Int. J. Earth Sci.* 90 (1), 77–87.
- Holyoke, C.W., Kronenberg, A.K., 2010. Accurate differential stress measurement using the molten salt cell and solid salt assemblies in the Griggs apparatus with applications to strength, piezometers and rheology. *Tectonophysics* 494, 17–31.
- Hubbert, K., Rubey, W.W., 1959. Role of fluid pressure in mechanics of overthrust faulting: I. Mechanics of fluid-filled porous solids and its application to overthrust faulting. *Geol. Soc. Am. Bull.* 70 (2), 115–166.
- Hunter, N.J.R., Weinberg, R.F., Wilson, C.J.L., Law, R.D., 2018. A new technique for quantifying symmetry and opening angles in quartz c-axis pole figures: implications for interpreting the kinematic and thermal properties of rocks. *J. Struct. Geol.* 112, 1–6.
- Jenkins, C.E., Bailey, C.M., Kunk, M., 2012. Argon thermochronology in the central Virginia Blue Ridge and piedmont. *Geol. Soc. Am. Abstr. Progr.* 44 (4).
- Kats, A., 1962. Hydrogen in alpha quartz. *Philips Res. Rep.* 17 (1–31), 133–195.
- Ketchum, R.A., 2005. Forward and inverse modeling of low-temperature thermochronometry data. *Rev. Mineral. Geochem.* 58 (1), 275–314.
- Ketchum, R.A., Gautheron, C., Tassan-Got, L., 2011. Accounting for long alpha-particle stopping distances in (U–Th–Sm)/He geochronology: refinement of the baseline case. *Geochim. Cosmochim. Acta* 75 (24), 7779–7791.
- Kidder, S., Avouac, J.P., Chan, Y.C., 2012. Constraints from rocks in the Taiwan orogen on crustal stress levels and rheology. *J. Geophys. Res.: Solid Earth* 117 (B9).
- Kilian, R., Heilbronner, R., Holyoke III, C.W., Kronenberg, A.K., Stünitz, H., 2016. Dislocation creep of dry quartz. *J. Geophys. Res.: Solid Earth* 121 (5), 3278–3299.
- Kjøll, H.J., Viola, G., Menegon, L., Sørensen, B.E., 2015. Brittle-viscous deformation of vein quartz under fluid-rich lower greenschist facies conditions. *Solid Earth* 6, 681–699.
- Koch, P.S., Christie, J.M., 1981. Spacing of deformation lamellae as a paleopiezometer. *EOS Translations American Geophysical Union* 62, 1030.
- Koch, N., Masch, L., 1992. formation of alpine mylonites and pseudotachylites at the base of the silvretta nappe, eastern alps. *Tectonophysics* 204 (3–4), 289–306.
- Kohlstedt, D.L., Evans, B., Mackwell, S.J., 1995. Strength of the lithosphere: constraints imposed by laboratory experiments. *J. Geophys. Res.: Solid Earth* 100 (B9), 17587–17602.
- Kronenberg, A.K., Wolf, G.H., 1990. Fourier transform infrared spectroscopy determinations of intragranular water content in quartz-bearing rocks: implications for hydrolytic weakening in the laboratory and within the earth. *Tectonophysics* 172 (3–4), 255–271.
- Kronenberg, A.K., Segall, P., Wolf, G.H., 1990. Hydrolytic weakening and penetrative deformation within a natural shear zone. *Geophysical Monograph* 56, 21–36.
- Kronenberg, A.K., Ashley, K.T., Francis, M.K., Holyoke, C.W., Jezek, L., Kronenberg, J. A., Law, R.D., Thomas, J.B., 2020. Water loss during dynamic recrystallization of Moine thrust quartzites. northwest Scotland: *Geology* 48. <https://doi.org/10.1130/G47041.1>.
- Kruhl, J.H., 1998. Reply: prism- and basal-plane parallel subgrain boundaries in quartz: a microstructural geothermobarometer. *J. Metamorph. Geol.* 16, 142–146.
- Küster, M., Stöckhert, B., 1999. High differential stress and sublithostatic pore fluid pressure in the ductile regime—microstructural evidence for short-term post-seismic creep in the Sesia zone, Western Alps. *Tectonophysics* 303 (1–4), 263–277.
- Lukert III, M.L., Nuckols II, E.B., 1976. Geology of the linden and flint hill quadrangles, Virginia: Virginia division of mineral Resources, report of investigations 44. scale 1, 24,000.
- Law, R.D., 2014. Deformation thermometry based on quartz c-axis fabrics and recrystallization microstructures: a review. *J. Struct. Geol.* 66, 129–161.
- Lisle, R.J., 1985. *Geological Strain Analysis: A Manual for the Rf/0 Technique*. Pergamon Press, p. 99.
- Lister, G.S., Hobbs, B.E., 1980. The simulation of fabric development during plastic deformation and its application to quartzite: the influence of deformation history. *J. Struct. Geol.* 2 (3), 355–370.
- Luan, F.C., Paterson, M.S., 1992. Preparation and deformation of synthetic aggregates of quartz. *J. Geophys. Res.* 97, 301–320.
- Mainprice, D., Bachmann, F., Hielscher, R., Schaeben, H., 2015. Descriptive tools for the analysis of texture projects with large datasets using MTEX: strength, symmetry and components. *Geol. Soc. Lond. Special Publ.* 409, 251–271.
- Menegon, L., Nasipuri, P., Stünitz, H., Behrens, H., Ravna, E., 2011. Dry and strong quartz during deformation of the lower crust in the presence of melt. *J. Geophys. Res.: Solid Earth* 116 (B10).
- Mercier, J.C., Anderson, D.A., Carter, N.L., 1977. Stress in the lithosphere: inferences from steady state flow of rocks. *Pure Appl. Geophys.* 115, 199–226.
- Milliken, K.L., Laubach, S.E., 2000. Brittle deformation in sandstone diagenesis as revealed by scanned cathodoluminescence imaging with application to characterization of fractured reservoirs. In: Chapter 9, *Cathodoluminescence in Geosciences*. Springer Verlag, New York, pp. 225–243.
- Mitra, S., 1976. A quantitative study of deformation mechanisms and finite strain in quartzite. *Contrib. Mineral. Petrol.* 59, 203–226.
- Mitra, S., 1978. Microscopic deformation mechanisms and flow laws in quartzites within the South Mountain anticline. *J. Geol.* 86 (1), 129–152.
- Mitra, G., 1979. Ductile deformation zones in Blue Ridge basement rocks and estimation of finite strains. *Geol. Soc. Am. Bull.* 90 (10), 935–951.
- Mitra, S., 1987. Regional variations in deformation mechanisms and structural styles in the central Appalachian orogenic belt. *Geol. Soc. Am. Bull.* 98 (5), 569–590.
- Mitra, S., Tullis, J., 1979. A comparison of intracrystalline deformation in naturally and experimentally deformed quartzite. *Tectonophysics* 53, T21–T27.
- Morgan, S.S., Law, R.D., 2004. Unusual transition in quartzite dislocation creep regimes and crystal slip systems in the aureole of the EJB pluton, California: a case for anhydrous conditions created by decarbonation of adjacent marbles. *Tectonophysics* 384, 209–231.
- Mosher, S., 1987. Pressure-solution deformation of the Purgatory Conglomerate, Rhode Island (USA): quantification of volume change, real strains and sedimentary shape factor. *J. Struct. Geol.* 9 (2), 221–232.
- Mulchrone, K.F., Meere, P.A., Choudhury, K.R., 2005. SAPE: a program for semi-automatic parameter extraction for strain analysis. *J. Struct. Geol.* 27 (11), 2084–2098.
- Naeser, C.W., Naeser, N.D., Newell, W.L., Southworth, S., Edwards, L.E., Weems, R.E., 2016. Erosional and depositional history of the Atlantic passive margin as recorded in detrital zircon fission-track ages and lithic detritus in Atlantic Coastal Plain sediments. *Am. J. Sci.* 316 (2), 110–168.
- Nakashima, S., Matayoshi, H., Yuko, T., Michibayashi, K., Masuda, T., Kuroki, N., Yamagishi, H., Ito, Y., Nakamura, A., 1995. Infrared microspectroscopy analysis of water distribution in deformed and metamorphosed rocks. *Tectonophysics* 245, 263–276.
- Newman, J., Mitra, G., 1993. Lateral variations in mylonite zone thickness as influenced by fluid-rock interactions, Linville Falls fault, North Carolina. *J. Struct. Geol.* 15, 849–863.
- O'Hara, K., 1988. Fluid flow and volume loss during mylonitization: an origin for phyllonite in an overthrust setting, North Carolina USA. *Tectonophysics* 156 (1–2), 21–36.
- O'Hara, K., 1990. State of strain in mylonites from the western Blue Ridge province, southern Appalachians: the role of volume loss. *J. Struct. Geol.* 12 (4), 419–430.
- Onasch, C.M., 1994. Assessing brittle volume-gain and pressure solution volume-loss processes in quartz arenite. *J. Struct. Geol.* 16 (4), 519–530.
- Onasch, C.M., Farver, J.R., Dunne, W.M., 2010. The role of dilation and cementation in the formation of cataclasis in low temperature deformation of well cemented quartz-rich rocks. *J. Struct. Geol.* 32 (12), 1912–1922.
- Palazzin, G., Raimbourg, H., Stünitz, H., Heilbronner, R., Neufeld, K., Precigout, J., 2018. Evolution in H<sub>2</sub>O contents during deformation of polycrystalline quartz: an experimental study. *J. Struct. Geol.* 114, 95–110.
- Passchier, C.W., Trouw, R.A., 2005. *Microtectonics*, second ed. Springer, Berlin, p. 366.
- Paterson, M.S., Luan, F.C., 1990. *Special Publications. Quartzite Rheology under Geological Conditions*, vol. 54. Geological Society, London, pp. 299–307, 1.
- Pfiffner, O.A., Ramsay, J.G., 1982. Constraints on geological strain rates – arguments from finite strain states of naturally deformed rocks. *J. Geophys. Res.* 87 (B1), 311–321.
- Post, A., Tullis, J., 1998. The rate of water penetration in experimentally deformed quartzite: implications for hydrolytic weakening. *Tectonophysics* 295 (1–2), 117–137.
- Rader, E.K., Biggs, T.H., 1975. *Geology of the Front Royal Quadrangle, Virginia: Virginia Division of Mineral Resources, Report of Investigations*, vol. 40 scale 1:24,000.
- Rahl, J.M., McGrew, A.J., Fox, J.A., Latham, J.R., Gabrielson, T., 2018. Rhomb-dominated crystallographic preferred orientations in incipiently deformed quartz sandstones: a potential paleostress indicator for quartz-rich rocks. *Geology* 46 (3), 195–198.
- Ramsay, J.G., 1967. *Folding and Fracturing of Rocks*. McGraw-Hill, New York, p. 568.
- Ramsay, J.G., Wood, D.S., 1973. The geometric effects of volume change during deformation processes. *Tectonophysics* 16 (3–4), 263–277.
- Reiners, P.W., Brandon, M.T., 2006. Using thermochronology to understand orogenic erosion. *Annu. Rev. Earth Planet Sci.* 34, 419–466.
- Reiners, P.W., Spell, T.L., Nicolescu, S., Zanetti, K.A., 2004. Zircon (U–Th)/He thermochronometry: He diffusion and comparisons with <sup>40</sup>Ar/<sup>39</sup>Ar dating. *Geochim. Cosmochim. Acta* 68 (8), 1857–1887.
- Ross, R.J., et al., 1982. *The Ordovician System in the United States: Correlation Chart and Explanatory Notes*. International Union of Geological Sciences, p. 73. Publication no. 12.
- Rutter, E.H., Brodie, K.H., 2004. Experimental intracrystalline plastic flow in hot-pressed synthetic quartzite prepared from Brazilian quartz crystals. *J. Struct. Geol.* 26 (2), 259–270.
- Schmid, S.M., Casey, M., 1986. Complete fabric analysis of some commonly observed quartz c-axis patterns. *Geophysical Monograph* 36 (6), 263–286.
- Shan, Y., 2008. An analytical approach for determining strain ellipsoids from measurements on planar surfaces. *J. Struct. Geol.* 30, 539–546.
- Shimamoto, T., Ikeda, Y., 1976. A simple algebraic method for strain estimation from ellipsoidal objects. *Tectonophysics* 36, 315–337.
- Sibson, R.H., 1977. Fault rocks and fault mechanisms. *J. Geol. Soc.* 133 (3), 191–213.
- Sibson, R.H., 1983. Continental fault structure and the shallow earthquake source. *J. Geol. Soc.* 140 (5), 741–767.
- Singleton, J.S., Wong, M.S., Johnston, S.M., 2018. The role of calcite-rich metasedimentary mylonites in localizing detachment fault strain and influencing the structural evolution of the Buckskin-Rawhide metamorphic core complex, west-central Arizona. *Lithosphere* 10, 172–193.

- Skemer, P., Katayama, I., Jiang, Z., Karato, S.I., 2005. The misorientation index: development of a new method for calculating the strength of lattice-preferred orientation. *Tectonophysics* 411 (1–4), 157–167.
- Smoot, J.P., Southworth, S., 2014. Volcanic rift margin model for the rift-to-drift setting of the late neoproterozoic-early cambrian eastern margin of laurentia: chilhowee Group of the appalachian Blue Ridge. *Geol. Soc. Am. Bull.* 126 (1–2), 201–218.
- Southworth, S., Aleinikoff, J.N., Bailey, C.M., Burton, W.C., Crider, E.A., Hackley, P.C., Smoot, J.P., Tollo, R.P., 2009. *Geologic Map of the Shenandoah National Park Region*. Open-File Report 2009–1153. U.S. Geological Survey, Virginia, p. 96, 1 plate, scale 1:100,000.
- Stanley, J.R., Flowers, R.M., 2016. Dating kimberlite emplacement with zircon and perovskite (U-Th)/He geochronology. *G-cubed* 1–17. <https://doi.org/10.1002/2016GC006519>.
- Stipp, M., Kunze, K., 2008. Dynamic recrystallization near the brittle-plastic transition in naturally and experimentally deformed quartz aggregates. *Tectonophysics* 448 (1–4), 77–97.
- Stipp, M., Tullis, J., 2003. The recrystallized grain size piezometer for quartz. *Geophys. Res. Lett.* 30 (21), 2088.
- Stipp, M., Stünitz, H., Heilbronner, R., Schmid, S.M., 2002. Dynamic recrystallization of quartz: correlation between natural and experimental conditions. *Geol. Soc. Lond. Special Publ.* 200 (1), 171–190.
- Stipp, M., Tullis, J., Behrens, H., 2006. Effect of water on the dislocation creep microstructure and flow stress of quartz and implications for the recrystallized grain size piezometer. *J. Geophys. Res.: Solid Earth* 111 (B4).
- Stöckhert, B., Brix, M.R., Kleinschrodt, R., Hurford, A.J., Wirth, R., 1999. Thermochronometry and microstructures of quartz—a comparison with experimental flow laws and predictions on the temperature of the brittle–plastic transition. *J. Struct. Geol.* 21 (3), 351–369.
- Stose, G.W., Miser, H.D., Katz, F.J., Hewett, D.F., 1919. Manganese deposits of the west foot of the Blue Ridge. *Virginia Geological Survey Bulletin* 17, 166.
- Tarantola, A., Diamond, L.W., Stünitz, H., 2010. Modification of fluid inclusions in quartz by deviatoric stress I: experimentally induced changes in inclusion shapes and microstructures. *Contrib. Mineral. Petrol.* 160, 825–843.
- Thomas, W.A., Gehrels, G.E., Greb, S.F., Nadon, G.C., Satkoski, A.M., Romero, M.C., 2017. Detrital zircons and sediment dispersal in the Appalachian foreland. *Geosphere* 13 (6), 2206–2230.
- Tokle, L., Hirth, G., Behr, W.M., 2019. Flow laws and fabric transitions in wet quartzite. *Earth Planet. Sci. Lett.* 505, 152–161.
- Trepmann, C.A., Stöckhert, B., 2003. Quartz microstructures developed during non-steady state plastic flow at rapidly decaying stress and strain rate. *J. Struct. Geol.* 25 (12), 2035–2051.
- Trepmann, C.A., Stöckhert, B., 2009. Microfabric of folded quartz veins in metagreywackes: dislocation creep and subgrain rotation at high stress. *J. Metamorph. Geol.* 27 (8), 555–570.
- Tullis, J., Christie, J.M., Griggs, D.R., 1973. Microstructures and preferred orientations of experimentally deformed quartzite. *Geol. Soc. Am. Bull.* 84, 297–314.
- Twiss, R.J., 1977. Theory and applicability of a recrystallized grain size paleopiezometer. *Pure Appl. Geophys.* 115, 227–244.
- van Daalen, M., Heilbronner, R., Kunze, K., 1999. Orientation analysis of localized shear deformation in quartz fibres at the brittle–ductile transition. *Tectonophysics* 303 (1–4), 83–107.
- Voll, G., 1976. Recrystallization of quartz, biotite and feldspars from Erstfeld to the Leventina Nappe, Swiss Alps, and its geological significance. *Schweiz. Mineral. Petrogr.* 56, 641–647.
- Vollmer, F.W., 1990. An application of eigenvalue methods to structural domain analysis. *Geol. Soc. Am. Bull.* 102 (6), 786–791.
- Vollmer, F.W., 2018. Automatic contouring of geologic fabric and finite strain data on the unit hyperboloid. *Comput. Geosci.* 115, 134–142.
- White, S., 1973. Deformation lamellae in naturally deformed quartz. *Nature Physical Science* 245 (141), 26–28.
- Wickham, J.S., 1972. Structural history of a portion of the Blue Ridge, northern Virginia. *Geol. Soc. Am. Bull.* 83 (3), 723–760.
- Wolfe, M.R., Stockli, D.F., 2010. Zircon (U–Th)/He thermochronometry in the KTB drill hole, Germany, and its implications for bulk He diffusion kinetics in zircon. *Earth Planet. Sci. Lett.* 295 (1–2), 69–82.